SE3Set: Harnessing Equivariant Hypergraph Neural Networks for Molecular Representation Learning

Hongfei Wu *
College of Chemistry and Molecular Engineering,
Peking University, Beijing, 100871, China

Lijun Wu
Microsoft Research AI4Science,
Beijing, 100084, China

Guoqing Liu
Microsoft Research AI4Science,
Beijing, 100084, China

Zhirong Liu *LiuZhiRong@pku.edu.cn*
College of Chemistry and Molecular Engineering,
Peking University, Beijing, 100871, China

Bin Shao *binshao@microsoft.com*
Microsoft Research AI4Science,
Beijing, 100084, China

Zun Wang *zunwang@microsoft.com*
Microsoft Research AI4Science,
Beijing, 100084, China

Reviewed on OpenReview: *https://openreview.net/forum?id=muWEt1TOyo*

Abstract

In this paper, we develop SE3Set, an SE(3) equivariant hypergraph neural network architecture tailored for advanced molecular representation learning. Hypergraphs are not merely an extension of traditional graphs; they are pivotal for modeling high-order relationships, a capability that conventional equivariant graph-based methods lack due to their inherent limitations in representing intricate many-body interactions. To achieve this, we first construct hypergraphs by proposing a new fragmentation method that considers both chemical and three-dimensional spatial information of the molecular system. We then design SE3Set, which incorporates equivariance into the hypergraph neural network. This ensures that the learned molecular representations are invariant to spatial transformations, thereby providing robustness essential for the accurate prediction of molecular properties. SE3Set has shown performance on par with state-of-the-art (SOTA) models for small molecule datasets like QM9 and MD17. It demonstrates outstanding performance on the MD22 dataset, achieving a remarkable 20% improvement in accuracy across all molecules. Furthermore, on the OE62 dataset, SE3Set outperforms all short-range models. We also conducted a detailed

*These authors did this work during an internship at Microsoft Research AI4Science.

analysis of OE62, highlighting the prevalence of complex many-body interactions in large molecules. This exceptional performance of SE3Set across diverse molecular structures underscores its transformative potential in computational chemistry, offering a route to more accurate and physically nuanced modeling. The code of this work is available at `https://github.com/Navantock/SE3Set`.

1 Introduction

Molecular representation (Mathews & Chaffee, 2012; David et al., 2020; Wigh et al., 2022) is pivotal for cheminformatics (Fourches et al., 2010), impacting the prediction of molecular properties in drug discovery and material science. Traditional descriptors like fingerprints capture basic structural and energetic aspects of molecules by considering mainly one- and two-body interactions. However, they often miss complex electronic correlations and collective behaviors important for understanding phenomena such as chemical reactivity and protein folding. To address this, advanced methods that include many-body interactions are crucial for a more comprehensive molecular characterization. These methods enhance the predictive capabilities of computational models by more accurately reflecting the intricate dynamics and properties of molecules, which are essential for a deeper understanding of their functionality and reactivity in cheminformatics.

Graph neural networks (GNNs) (Zhou et al., 2020; Wu et al., 2020) are a foundational tool for representing structured data in molecular sciences with atoms as nodes and chemical bonds as edges, respectively. GNN models excel in tasks ranging from property prediction to reaction simulation (Do et al., 2019; Xiong et al., 2021; Reiser et al., 2022). GNNs can capture higher-order molecular interactions through message passing (Gilmer et al., 2017) but face overfitting and inefficiency challenges (Godwin et al., 2021; Rusch et al., 2023). Architectural improvements in GNNs facilitate the modeling of complex interactions, overcoming some limitations of deep networks (Gasteiger et al., 2019; Schütt et al., 2021; Batzner et al., 2022). Advances demonstrate the potential of architectural enhancements in GNNs to represent complex interactions (Gasteiger et al., 2020; 2021; Thölke & De Fabritiis, 2021; Batatia et al., 2022; Musaelian et al., 2023; Wang et al., 2024), but efficiently integrating many-body interactions into these networks is an ongoing challenge (Wang et al., 2023).

An effective approach to describe many-body interactions in chemical molecules involves leveraging predefined substructures, such as functional groups in organic chemistry. This strategy has demonstrated significant success in various chemical molecule-related tasks, including pre-training (Li & Jiang, 2021; Li et al., 2023) and representation learning (Hajiabolhassan et al., 2023; Wu et al., 2023). Furthermore, these predefined chemical substructures can be naturally modeled as hyperedges within a hypergraph structure. Hypergraphs offer a compelling alternative to complex GNN architectures. Hypergraphs, with hyperedges connecting multiple vertices, can naturally represent many-body phenomena like electronic delocalization and collective vibrations. This allows for a more accurate modeling of molecular intricacies beyond the limitations of traditional graphs. Integrating hypergraphs with machine learning, particularly through Hypergraph Neural Networks (HGNNs), is an emerging research area. HGNNs manage the flow of information across hyperedges, capturing complex multi-atom interactions and enriching molecular representations. This technique promises to balance model expressiveness with computational efficiency. By innately encoding many-body interactions, HGNNs stand to significantly advance cheminformatics, offering a new approach to molecular property prediction and simulation that resonates with the actual behavior of chemical systems.

By leveraging the relationship between hypergraphs and many-body interactions, we aim to incorporate the advantages of equivariant graph neural networks into hypergraph structure learning, thereby developing a more comprehensive molecular representation learning model grounded in domain knowledge. In this work, we introduce SE3Set, an innovative approach that enhances traditional GNNs by exploiting hypergraphs for modeling many-body interactions, while ensuring SE(3) equivariant representations that remain consistent regardless of molecular orientation. Our key contributions are:

- A new fragmentation method for hypergraph construction that seamlessly integrates 2D chemical and 3D spatial information, enriching the molecular structure representation.

- The deployment of hypergraph neural networks to capture many-body interactions, providing a deeper insight into molecular behavior that surpasses conventional pairwise modeling.
- The incorporation of SE(3) equivariance within our hypergraph framework, guaranteeing orientation-independent molecular representations.
- SE3Set underwent a comprehensive benchmarking process, exhibiting comparable outcomes to state-of-the-art (SOTA) models on small molecule datasets QM9 and MD17. It demonstrated exceptional performance on the larger molecule dataset MD22, where higher-order interactions are more evident, surpassing SOTA models with a significant reduction in mean absolute errors (MAEs) by an average of roughly 20%. This confirms SE3Set's efficacy in capturing the complexity of molecular representations.

These advances establish SE3Set as a formidable tool for molecular representation learning, with implications for computational chemistry and beyond.

2 Related works

2.1 Graph neural networks

Message passing neural networks (MPNNs), a class of graph neural networks, are essential for learning node features by transmitting information along graph edges, a process crucial for interpreting structured data like molecules (Gilmer et al., 2017). Equivariant GNNs are especially important for molecular modeling. They adopt either group representation methods, aligning architectures to symmetry groups for improved interaction modeling (Thomas et al., 2018; Anderson et al., 2019; Fuchs et al., 2020; Batzner et al., 2022; Liao & Smidt, 2022; Liao et al., 2023; Musaelian et al., 2023), or direction-based methods that incorporate spatial information for accurate molecular representations (Schütt et al., 2017; Kindermans & Müller, 2018; Coors et al., 2018; Gasteiger et al., 2019; 2020; Schütt et al., 2021; Thölke & De Fabritiis, 2021; Gasteiger et al., 2021; Wang et al., 2022; Du et al., 2024; Aykent & Xia, 2024; Wang et al., 2024) and have been engineered to handle intricate up to five-body interactions (Wang et al., 2023).

2.2 Hypergraph neural networks

Hypergraph Neural Networks (HGNNs) enhance GNNs by incorporating multi-node hyperedges to better capture complexity in data from various domains. They advance GNNs' implicit many-body interactions with methods like clique expansion for compatibility with existing algorithms (Agarwal et al., 2005; Zhou et al., 2006) and employ tensor techniques for improved hypergraph-based feature learning (Li et al., 2013; Pearson & Zhang, 2014; Benson et al., 2017; Chien et al., 2021a; Tudisco et al., 2021). While equivariant HGNNs adeptly handle node permutations, preserving data symmetries (Kim et al., 2021; 2022a), they often miss 3D spatial transformations, crucial for physical system modeling. In computational chemistry, hypergraph algorithms simulate complex behaviors and optimize molecules through hypergraph grammar (Cui et al., 2023; Tavakoli et al., 2022; Kajino, 2019), providing multidimensional insights into molecular structures (Nachmani & Wolf, 2020; Chen et al., 2021; Chen & Schwaller, 2023). Despite their promise, these methods still face hurdles in integrating spatial information effectively.

2.3 Fragmentation methods

Fragmentation methods break down complex molecules for simpler *ab initio* QM computations of properties, later combining these for a holistic view (Gordon et al., 2012; Collins & Bettens, 2015). Leveraging the localized nature of chemical reactions, these techniques aim for scalable algorithms suitable for large molecule analysis. While instrumental in computational pretraining (Du et al., 2021; Kim et al., 2022b; Luong & Singh, 2023), they typically neglect the fusion of 2D structures and 3D spatial data. Hence, we advocate for a refined fragmentation approach that merges chemical properties with spatial context, potentially advancing hypergraph-based chemical modeling.

3 Preliminaries

3.1 Equivariance

Consider a function $\mathcal{L}$ that maps inputs from space $\mathcal{X}$ to outputs in space $\mathcal{Y}$. $\mathcal{L}$ is called G-equivariant if it preserves the symmetry of a group G across mappings, meaning for each $g \in G$, we have:

$$\mathcal{L} \circ D^{\mathcal{X}}(g) = D^{\mathcal{Y}}(g) \circ \mathcal{L}, \tag{1}$$

where $D^{\mathcal{X}}$ represents the group G's action on $\mathcal{X}$. This ensures that the function $\mathcal{L}$ reflects changes made to inputs by G in its outputs.

3.2 Hypergraph

Hypergraphs elegantly capture the essence of higher-order interactions among multiple entities, making them an invaluable tool for representing complex relational data. Let $\mathcal{G} = (V, E)$ be a hypergraph with N vertices and M hyperedges, where V represents a set of nodes and E is a set of hyperedges. Distinguishing itself from a traditional graph, a hyperedge can encompass multiple nodes, not limited to two, i.e. each hyperedge $e \in E$ is a non-empty subset of V.

3.3 AllSet

The AllSet framework (Chien et al., 2021b), an advanced HGNN model, addresses heuristic propagation rule limitations in HGNNs by integrating Deep Sets (Zaheer et al., 2017) and Set Transformers (Lee et al., 2019) principles. It uses task-optimized dual multiset functions that maintain permutation invariance, crucial for hypergraph learning. The update rules in AllSet are:

$$Z_{e,:}^{(t+1),v} = f_{\mathcal{V}\to\mathcal{E}}(V_{e\setminus v, X^{(t)}}; Z_{e,:}^{(t),v}, X_{v,:}^{(t)}), \tag{2}$$

$$X_{v,:}^{(t+1)} = f_{\mathcal{E}\to\mathcal{V}}(E_{v, Z^{(t+1),v}}; X_{v,:}^{(t)}). \tag{3}$$

Here, $f_{\mathcal{V}\to\mathcal{E}}$ and $f_{\mathcal{E}\to\mathcal{V}}$ are the key multiset functions mapping node and hyperedge features. For example, $f_{\mathcal{V}\to\mathcal{E}}(S) = \text{MLP}\left(\sum_{s\in S} \text{MLP}(s)\right)$ is used in AllDeepSets. The notation $V_{e,X}$ and $E_{v,Z}$ represent multisets of node and hyperedge features, respectively. The AllSet approach updates nodes and hyperedges in the hypergraph by leveraging their features in conjunction with those of adjacent hyperedges or nodes, enabling a rich representation of the hypergraph structure. The method could differentiate node v from its multiset, allowing for sophisticated feature aggregation.

4 Methods

We introduce the SE3Set model to leverage hypergraph neural networks for capturing complex molecular interactions, integrating both 2D chemical and 3D spatial structures (Sec. 4.1). It builds upon the AllSet framework (Chien et al., 2021b) and the Equiformer (Liao & Smidt, 2022). Upcoming sections will delve into the specifics of molecular fragmentation and the SE3Set architecture.

4.1 Fragmentation algorithm

To harness the power of hypergraph neural networks for molecular representations, we need to map molecules onto hypergraph structures through a refined fragmentation algorithm. Our strategy intertwines molecular topology and spatial geometry to create hyperedges that capture groups of atoms, reflecting their functional and spatial characteristics. More specifically, the topology incorporates the chemical definitions of covalent bonds, functional groups, etc., allowing us to initially delineate fragments by chemical prior knowledge of chemistry to identify the important substructures. And the 3D spatial structure aids in modifying the fragments to capture the interactions in short range which are not specified by covalent bonds in the conformation. Thus, in crafting this fragmentation approach for hypergraph-based molecular representation, we propose a set of principles for a fragmentation approach:

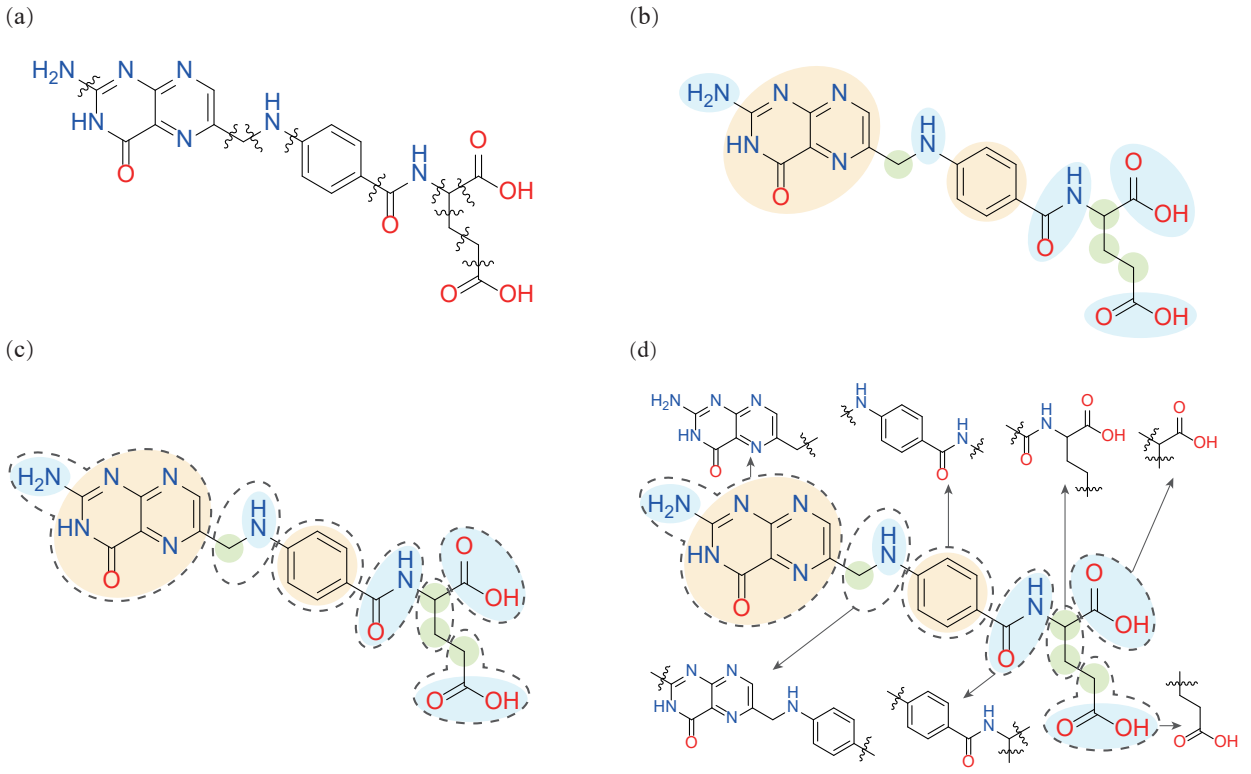

Figure 1: Folic acid fragmentation illustrated with CID 135398658 from PubChem. (a) Preprocessing to identify cleavable bonds for fragmentation. (b) Initial fragments formed using BFS, color-coded by functional groups (blue), rings (orange), and single atoms (green). (c) Fragments merged to satisfy atom count criteria, detailed in Appendix C (d) Expansion of fragments shown with directional arrows.

1. The design should merge topological chemistry with 3D structural data into a unified hypergraph representation, ensuring hyperedges accurately embody the molecule's chemical and spatial properties.

2. Controlling fragment size is vital for the SE3Set model to balance capturing meaningful interactions and computational efficiency. Optimal fragment sizes are key for model performance and learning capabilities.

3. To preserve the key chemical information for the molecule's properties and behavior, the fragmentation better only selectively break single bonds and maintain important functional groups and ring integrity.

4. Fragment overlap is essential to maintain functional group effects on local charge distribution and to ensure hyperedge interaction within the SE3Set model for improved molecular learning.

Based on these principles, we propose a fragmentation method for molecules combined with chemical-defined substructures whose definitions and usages are described in detail in Appendix A. Generally, our fragmentation algorithm improves molecular representations by combining bond order, functional groups, and substructures, including SMARTS-identified smaller rings and merged adjacent groups. Overcoming the drawbacks of non-overlapping fragmentation, it uses 3D spatial data and allows overlaps, preserving local effects for precise charge distribution and enhancing hypergraph neural network learning of molecular interactions.

Definition 4.1. A molecular fragment, denoted as $\mathfrak{F}$, is defined as a specific subset of atoms within a molecule, characterized by being a cohesive assembly of predefined substructures linked in a sequential concatenation.

Our fragmentation method meticulously dissects a given molecule into meaningful subsets of atoms, and this process unfolds through four steps (corresponding to the pipeline in Fig. 1):

1. Pre-processing by analyzing the molecule's bond order matrix to mask high-order bonds and those within functional groups or rings, and merging adjacent functional groups for a streamlined structural representation.
2. Core substructures are delineated from the remaining bonds using a Breadth-First Search algorithm, establishing the basic units of the molecular framework.
3. These substructures are then aggregated into larger molecular fragments according to predefined rules that maintain a minimum atom count within each fragment. This step could be optional.
4. To enhance fragment connectivity, we expand each by incorporating adjacent groups, using interaction strength metrics based on interatomic distances to guide this process. Here we set the cutoff value denoted as c_w of an interaction strength metric to intercept the extended fragment.

Furthermore, step 4 leads to a substantial computational overhead for hypergraph neural networks when processing larger molecular systems. To enhance the efficiency of our model for such expansive molecular systems, we introduce a revised strategy for step 4:

4* For each atom i, identify the neighboring atoms $\mathcal{N}_i$ that fall within a specified radial cutoff r_c. A fragment $\mathfrak{F}$ is considered to be adjacent to atom i if there is an overlap of at least one atom between $\mathfrak{F}$ and $\mathcal{N}_i$. For ease of reference, the set of fragments adjacent to atom i is represented as $\mathcal{N}_i^{\mathcal{F}}$, which implies that $\mathcal{N}_i^{\mathcal{F}} = \{\mathfrak{F} | \mathfrak{F} \cap \mathcal{N}_i \neq \varnothing\}$.

We designate the application of step 4 as an explicit overlap and the application of step 4* as an implicit overlap. These approaches introduce nuanced variations in the mathematical expressions of our model, as reflected in Eq. 8, Eq. 9, and Eq. 16. For the detailed step-by-step methodology, please refer to Appendix A.

4.2 SE3Set

Building upon our aforementioned fragmentation algorithm, we now turn to outline the architecture of SE3Set. The SE3Set model, influenced by AllSet (Chien et al., 2021b) and built on the Equiformer (Liao & Smidt, 2022), incorporates 3D spatial equivariance (proof refers to Appendix E) in our hypergraph neural network, improving the capture of many-body interactions for precise molecular structure representation. SE3Set consists of an embedding layer, attention blocks, and an output head, as shown in Fig. 2 (a). Moreover, we give a brief discussion in Appendix K on the advantages of the hypergraph structure we implement when considering the efficiency of message passing, comparing with the vanilla graph neural networks using a simple illustrative example.

4.2.1 Embedding

As depicted in Fig. 2 (b), the embedding block generates detailed node and hyperedge features reflecting molecular structures. Node features blend intrinsic properties with degree embeddings from connected hyperedges, while hyperedge features aggregate node embeddings and the corresponding relative position vectors depending on the node on which the hyperedge feature is located. SH (Spherical Harmonic) functions are used to project normalized relative position vectors $\vec{r}_{ij}$ between node i and j into the irreducible representations (irreps) feature space with different orders l, i.e. $\mathrm{SH}(\vec{r}_{ij}) = Y^l\left(\frac{\vec{r}_{ij}}{\|\vec{r}_{ij}\|}\right)$. The features are also mapped onto the same l-order irreps space for SE3 equivariance and updated separately. Hyperedges capture nodes' positional relationships, assigning a distinct feature h_i^{α} to each node i in hyperedge $\mathfrak{F}_{\alpha}$, reinforcing structural fidelity. Nodes x_i integrate hyperedge information, harmonizing uniqueness with interconnections. Attention mechanisms then refine node and hyperedge interactions for accurate molecular and structural representation.

4.2.2 Equivariant hypergraph attention blocks

As presented in Fig. 2 (c)-(f), the attention mechanism comprises two essential components: the Vertex-to-Edge (V2E) and Edge-to-Vertex (E2V) attention blocks, based on the AllSet framework (Chien et al., 2021b).

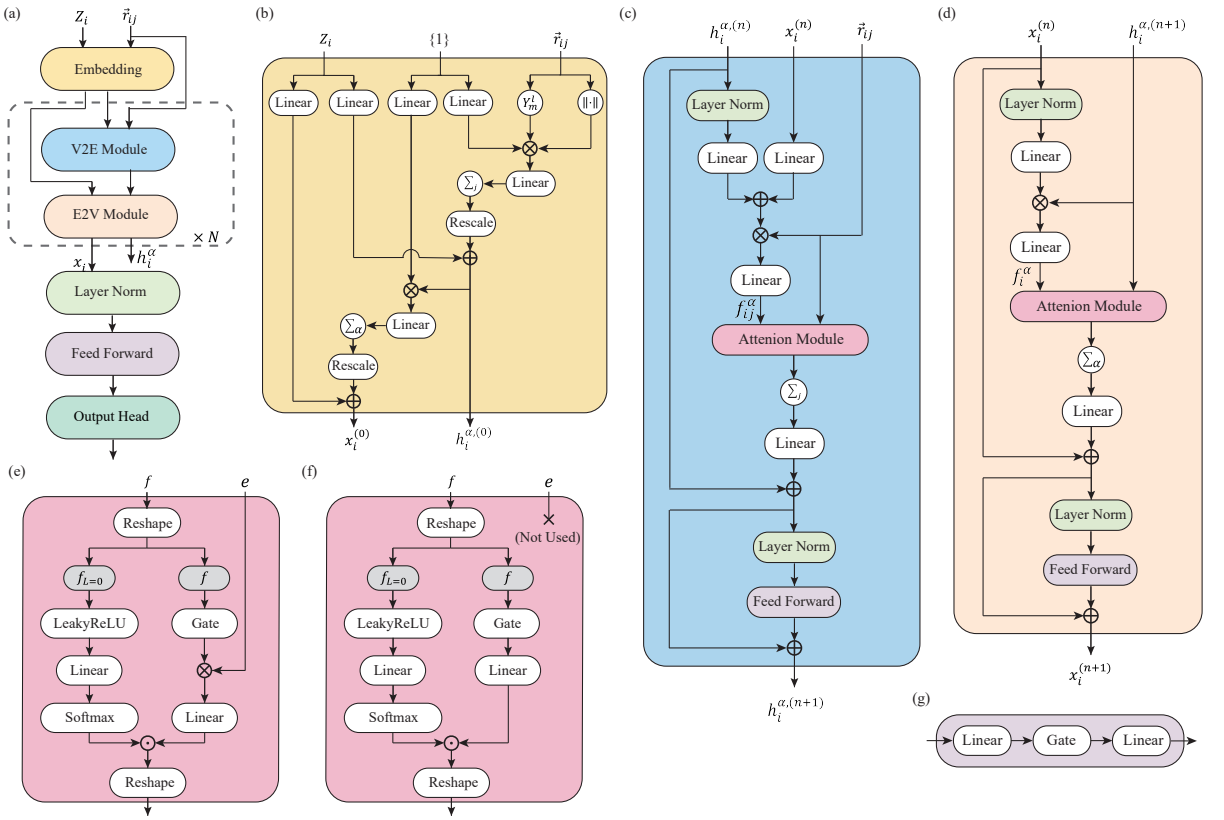

Figure 2: Overall architecture of SE3Set. (a) SE3Set begins with node and hyperedge embeddings, cycles through V2E and E2V attention modules for iterative updates, and concludes with normalization and a feed-forward block for output. (b) Embedding. Atomic numbers and position vectors are transformed into initial embeddings for nodes and hyperedges. (c) V2E Module. Utilizes node features and their relative positions to update hyperedge features. (d) E2V Module. Employs hyperedge features to refresh node features. (e) Attention Block. Merges feature sets with positional or hyperedge data for feature processing. (f) A variant of the Attention Module in E2VModule. This Attention Module does not introduce hyperedge information itself. This architecture corresponds to the result of E2V Summation in ablation study 5.4. (g) Feed-Forward Block. Enhances feature sets through a streamlined network. Symbols $\otimes$, $\oplus$, and $\odot$ in figures denote depth-wise tensor product, summation, and Hadamard multiplication, respectively. h_i^{α} represents hyperedge features, x_i is for node features, superscript n indicates the number of updates, and $\vec{r}_{ij}$ is the relative position vector between nodes i and j.

The V2E block refines hyperedge features, while the E2V block updates node features, both operating with an equivariant hypergraph attention mechanism. To improve training and enable deeper network structures, we incorporate normalization layers and residual connections to prevent gradient issues. The attention module's output passes through a feed-forward block (Fig. 2 (d)), enhancing representation complexity. Node and hyperedge features maintain equivariance to molecular geometry, preserving data symmetries and the integrity of representations, thus boosting the model's expressiveness in capturing complex structural interactions. (The concepts of irreducible representations and tensor products can be referenced in the Appendix F.)

V2E attention The SE3Set model uses geometrically invariant attention weights a_{ij}, derived from $l = 0$ irreps acting as scalars under geometric transformations. These weights are computed from scalar features $f_{ij,l=0}$ using an MLP with LeakyReLU activation and softmax normalization, reflecting node relationships within the hypergraph. Node and hyperedge features undergo non-linear transformations represented by tensor products of irreps with the quantum number l. The features combine through direct tensor products (DTP), yielding non-linear values v_{ij} (Fig. 2 (c)). Hyperedge features are updated by aggregating features

from connected nodes, utilizing SH and radial basis functions on hyperedge features. The model calculates initial features f_{ij}^{α} and V2E attention weights a_{ij}^{α} via MLPs, with non-linear values v_{ij}^{α} emerging from similar transformations.

$$t_{ij}^{\alpha} = (\text{Linear}(x_i) + \text{Linear}(x_j)) \tag{4}$$

$$f_{ij}^{\alpha} = \text{Linear}(t_{ij}^{\alpha} \otimes_{w(\|\vec{r}_{ij}\|)}^{\text{DTP}} \text{SH}(\vec{r}_{ij})) \tag{5}$$

$$a_{ij}^{\alpha} = \text{Softmax}_j(a^{\top}\text{LeakyReLU}(f_{ij,l=0}^{\alpha})) \tag{6}$$

$$v_{ij}^{\alpha} = \text{Linear}(\text{Gate}(f_{ij}^{\alpha}) \otimes_{w(\|\vec{r}_{ij}\|)}^{\text{DTP}} \text{SH}(\vec{r}_{ij})) \tag{7}$$

Ultimately, the SE3Set model updates hyperedge features h_i^k by accumulating the weighted features of nodes within the same hyperedge and applying a linear transformation to the aggregated information. For the explicit overlap fragmentation method,

$$\Delta h_i^{\alpha} = \text{Linear}\left(\sum_{j:n_i \in \mathfrak{F}_{\alpha} \wedge n_j \in \mathfrak{F}_{\alpha}} a_{ij}^{\alpha} v_{ij}^{\alpha}\right) \tag{8}$$

where n_i denotes the node with index i and $\mathfrak{F}_{\alpha}$ denotes the fragment with index α as each fragment could be considered as a hyperedge in the hypergraph. Due to the frequent occurrence of a high number of explicitly overlapping atoms, this scenario commonly results in increased computational complexity. Consequently, when adopting the implicit overlap approach, we may opt for an equation of the form:

$$\Delta h_i^{\alpha} = \text{Linear}\left(\sum_{j:j \in \mathfrak{F}_{\alpha} \wedge \mathfrak{F}_{\alpha} \in \mathcal{N}_i^{\mathcal{F}}} a_{ij}^{\alpha} v_{ij}^{\alpha}\right) \tag{9}$$

where $\mathcal{N}_i^{\mathcal{F}}$ is delineated in step 4* of the implicit overlap method. This characteristic renders it a more computationally efficient scheme for Vertex-to-Edge (V2E) attention mechanisms. The detailed architecture of the V2E attention block is shown in Fig. 2 (c) and (e).

E2V attention Following the V2E attention module, the E2V attention module (Fig. 2 (f)) updates node features by transforming them with a tensor product of the updated hyperedge feature, followed by a linear layer. Attention weights are then calculated using softmax-applied, LeakyReLU-activated features, ensuring node features are refined after hyperedge updates.

$$f_i^{\alpha} = \text{Linear}((\text{Linear}(x_i) \otimes^{\text{DTP}} h_i^{\alpha}) \tag{10}$$

$$a_i^{\alpha} = \text{Softmax}_{\alpha}(a^{\top}\text{LeakyReLU}(f_{i,l=0}^{\alpha})) \tag{11}$$

These attention weights direct the synthesis of information, culminating in the calculated value:

$$v_i^{\alpha} = \text{Linear}(\text{Gate}(f_i^{\alpha}) \otimes^{\text{DTP}} h_i^{\alpha}). \tag{12}$$

Furthermore, we propose an alternative method for constructing the E2V attention block as shown in Fig. 2 (g).

$$f_i^{\alpha} = \text{Linear}(\text{Linear}(x_i) + \text{Linear}(h_i^{\alpha})) \tag{13}$$

$$a_i^{\alpha} = \text{Softmax}_{\alpha}(a^{\top}\text{LeakyReLU}(f_{i,l=0}^{\alpha})) \tag{14}$$

$$v_i^{\alpha} = \text{Linear}(\text{Gate}(f_i^{\alpha})) \tag{15}$$

However, practical experiments reveal that the previous method yields superior results, with detailed findings presented in Sec. 5.4.

Then the node aggregates all the hyperedge features corresponding to itself to update the node feature,

$$\text{Explicit overlap: } \Delta x_i = \text{Linear}\left(\sum_{\alpha: i \in \mathfrak{F}_\alpha} a_i^\alpha v_i^\alpha\right), \tag{16}$$

$$\text{Implicit overlap: } \Delta x_i = \text{Linear}\left(\sum_{\alpha: \mathfrak{F}_\alpha \in \mathcal{N}_i^{\mathcal{F}}} a_i^\alpha v_i^\alpha\right) \tag{17}$$

The visualized architecture of the E2V attention block is also shown in Fig. 2 (d), (e), and (f).

4.2.3 Output head

The SE3Set model employs node features to generate predictions, using a feed-forward network to transform these features into the target label's irreps dimension. A summation strategy aggregates node features into a single hypergraph-level representation, which is then processed by a linear layer to output the model's final predictions.

5 Results

We tested our equivariant hypergraph neural network on QM9 (Ruddigkeit et al., 2012; Ramakrishnan et al., 2014), MD17 (Chmiela et al., 2017) (see Appendix G), MD22 (Chmiela et al., 2023), and OE62 (Stuke et al., 2020) to assess its molecular representation learning. QM9 and MD17 gauge small molecule property prediction, while MD22 and OE62 evaluate larger systems with complex many-body interactions (Wang et al., 2023). An ablation study was also conducted to pinpoint the contributions of fragmentation and architecture to our method's performance, offering insights into the network's efficacy and areas for enhancement. In the Appendix H, we have also provided a detailed analysis of the model's complexity. Additionally, we have evaluated the robustness of our model on different tasks by some summary statistic metrics in Appendix M.

5.1 QM9

The QM9 dataset (Ruddigkeit et al., 2012; Ramakrishnan et al., 2014) consists of 134k small organic molecules calculated at the B3LYP/6-31G(2df, p) level. SE3Set, after training on 110k QM9 molecules and validation on 10k, achieves low mean absolute errors (MAEs) in 12 tasks, performing on par with leading models, as detailed in Table 1. For completeness, some pre-trained molecular representation learning models are also selected as baselines (see Appendix J). In small molecular systems, higher-order many-body interactions are less pronounced and the molecular properties can be well approximated by the GNN-based models designed with some of the higher-order interactions. As a result, SE3Set does not significantly outperform other state-of-the-art (SOTA) models. Nevertheless, we will demonstrate that, while SE3Set maintains good performance with small molecules, the rate of performance degradation significantly decreases as the size of the molecules increases (see Section 5.3).

5.2 MD22

Recognizing the prominence of higher-order many-body interactions in larger molecules (Wang et al., 2023), SE3Set was tested on the comprehensive MD22 dataset (Chmiela et al., 2023). This dataset spans four classes of biomolecules and supramolecules, from a 42-atom peptide to a 370-atom nanotube, with high-resolution sampling at 400-500 K using the PBE+MBD (Perdew et al., 1996; Tkatchenko et al., 2012) framework for energy and force computations. Our fragmentation method, which maintains functional groups and rings, selectively excludes structures like the Buckyball catcher and Double-walled nanotube from MD22, thus concentrating on the other five molecular types. We partition the training/test set following QuinNet (Wang et al., 2023). As Table 2 shows, SE3Set outperforms other SOTA models in these cases, reducing MAEs by an average of 20%, underscoring its exceptional ability to capture molecular intricacies. Moreover, our results indicate that incorporating higher-order many-body interactions is crucial for representing the non-local features of larger molecules within the MD22 dataset.

Table 1: A comparative analysis was performed to assess the Mean Absolute Errors (MAEs) on the QM9 dataset when training SE3Set on a configuration comprising 110,000 training samples and 1,000 validation samples. Bolding shows the best model and the underlining shows the second best model and the underlining tilde shows third best model. All the baseline results are extracted from the origin papers (Schütt et al., 2017; Gasteiger et al., 2020; Schütt et al., 2021; Coors et al., 2018; Wang et al., 2022; Thölke & De Fabritiis, 2021; Musaelian et al., 2023; Wang et al., 2024; Liao & Smidt, 2022; Wang et al., 2023).

	UNIT	SCHNET	DIMENET++	PAINN	SPHERENET	COMENET	ET	ALLEGRO	VISNET	QUINNET	EQUIFORMER	SE3SET
μ	D	0.033	0.030	0.012	0.026	0.0245	0.011	-	**0.010**	0.771	0.011	0.011
α	a_0^3	0.235	0.044	0.045	0.046	0.0452	0.059	-	**0.041**	0.047	0.046	0.045
HOMO	meV	41	25	20	23	23	20	-	17.3	20.4	**15**	**15**
LUMO	meV	34	20	28	18	20	18	-	14.8	17.6	14	**13**
GAP	meV	63	33	46	32	32	36	-	31.7	**28.2**	30	29
R^2	a_0^2	0.073	0.331	0.066	0.292	0.259	0.033	-	**0.030**	0.194	0.251	0.197
ZPVE	meV	1.70	1.21	1.28	**1.12**	1.20	1.84	-	1.56	1.26	1.26	1.40
U_0	meV	14	6	5.85	6	6.59	6.15	4.7	**4.23**	7.6	6.59	5.74
U	meV	19	6	5.83	7	6.82	6.38	4.4	**4.25**	8.4	6.74	5.69
H	meV	14	7	5.98	6	6.86	6.16	**4.4**	4.52	7.8	6.63	5.70
G	meV	14	8	7.35	8	7.98	7.62	**5.7**	5.86	8.5	7.63	6.63
C_v	$\frac{\text{kcal}}{\text{mol·K}}$	0.033	0.023	0.024	**0.021**	0.024	0.026	-	0.023	0.024	0.023	0.025

Table 2: A comparison of Mean Absolute Errors (MAEs) across various benchmarked models. SE3Set is trained on the five molecules of the MD22 dataset with a specific number of training/validation. Bolding shows the best model and underlining shows the second best model. The improvements column shows the improvement of our model over the previous SOTA model in percentage terms. The MAEs reflect the precision of energy predictions in units of kcal/mol and forces in units of kcal/(mol·Å). The results of the baseline models refer to the origin papers (Chmiela et al., 2023; Thölke & De Fabritiis, 2021; Musaelian et al., 2023; Batatia et al., 2022; Liao & Smidt, 2022; Wang et al., 2024; 2023; Li et al., 2024).

MOLECULE	# TRAIN/VAL		SGDML	TORCHMD-NET	ALLEGRO	MACE	EQUIFORMER	VISNET	QUINNET	EQUIFORMER-LSRM	VISNET-LSRM	SE3SET	IMPROVEMENTS
AC-ALA3-NHME	5500/500	ENERGY	0.3902	0.1121	0.1019	0.0620	0.0828	0.0796	0.084	0.0780	0.0654	**0.0499**	19.5%
		FORCE	0.7968	0.1879	0.1068	0.0876	0.0804	0.0972	0.0681	0.0877	0.0902	**0.0545**	20.0%
DHA	7500/500	ENERGY	1.3117	0.1205	0.1153	0.1317	0.1788	0.1526	0.12	0.0878	0.0873	**0.0826**	5.4%
		FORCE	0.7474	0.1209	0.0732	0.0646	0.0506	0.0668	0.0515	0.0534	0.0598	**0.0360**	28.9%
STACHYOSE	7500/500	ENERGY	4.0497	0.1393	0.2485	0.1244	0.1404	0.1283	0.23	0.1252	0.1055	**0.0762**	27.8%
		FORCE	0.6744	0.1921	0.0971	0.0876	0.0635	0.0869	0.0543	0.0632	0.0767	**0.0424**	21.9%
AT-AT	2500/500	ENERGY	0.7235	0.1120	0.1428	0.1093	0.1309	0.1688	0.14	0.1007	0.0772	**0.0585**	24.2%
		FORCE	0.6911	0.2036	0.0952	0.0992	0.0960	0.1070	0.0687	0.0811	0.0781	**0.0556**	19.1%
AT-AT-CG-CG	1500/500	ENERGY	1.3885	0.2072	0.3933	0.1578	0.1510	0.1995	0.38	0.1335	0.1135	**0.1002**	11.7%
		FORCE	0.7028	0.3259	0.1280	0.1153	0.1252	0.1563	0.1273	0.1065	0.1063	**0.0825**	22.4%

5.3 OE62

The OE62 dataset (Stuke et al., 2020) contains about 62k large organic molecules with annotated DFT-computed energies in the unit of eV. We randomly selected 50,000 data points as the training set and 6,000 data points as the validation set following the work of Kosmala et al. (2023). Here we report the MAE of energy as the performance metric on the test dataset. Since OE62 is considered to have significant long-range interactions (Kosmala et al., 2023), we selected model results without explicit long-range modeling as a baseline. The results (Table 3) demonstrate that SE3Set outperforms all baseline models (which focus on short-range interactions), highlighting the potential of our model for capturing many-body interactions.

To further evaluate the performance of our model, we conducted additional tests on the OE62 dataset to analyze the correlation between model performance (SE3Set and the baseline models) and molecular size, as reflected by the number of atoms in a molecule. First, we reproduced the results of the baseline model using open-source code[1], as shown in parentheses in the Table 3. The reproduced results are largely consistent with those extracted from the original work. The analysis of each model's performance in representing molecules of different sizes is illustrated in Fig. 3. We grouped the test set based on the number of atoms in the molecules and reported the MAE for each group. To facilitate a clearer comparison among different models, we defined the relative difference (RD) metric across all m models.

$$\text{RD}_m = \frac{\text{MAE}_m - \frac{1}{M}\sum_m \text{MAE}_m}{\frac{1}{M}\sum_m \text{MAE}_m} \tag{18}$$

[1] https://github.com/arthurkosmala/EwaldMP

Table 3: A comparison of MAEs across some benchmarked models on OE62 dataset in the unit of meV. The result of the best model is bolded. The baseline results are extracted from Ref. Kosmala et al. (2023), while the results in parentheses represent the reproduced experimental outcomes.

Model	SchNet	PaiNN	DimeNet++	GemNet-T	SE3Set(3 Layers)
MAE (meV)	131.3 (130.0)	63 (62.6)	53.8 (52.3)	53.1 (54.9)	**51.7**

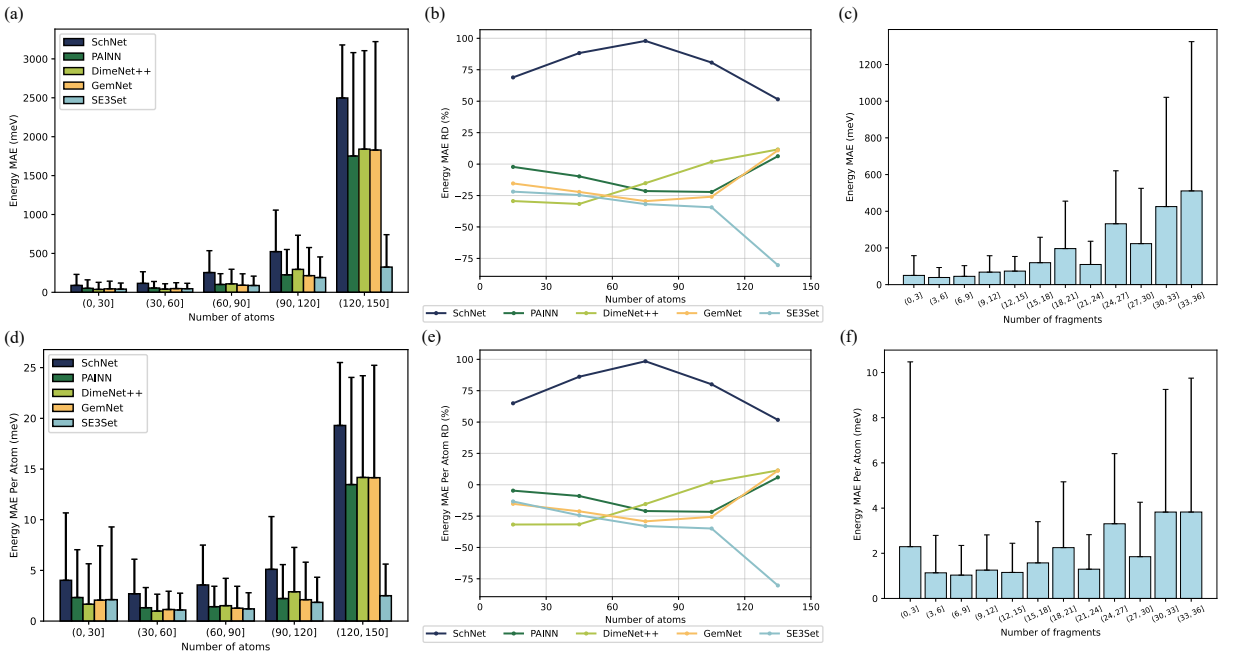

Figure 3: The correlation between the mean absolute error (MAE) of energy predictions by different SE3Set models and varying molecular sizes or fragment counts. We use the number of atoms to represent molecular size, dividing them into bins at intervals of 30 atoms. For each interval, we calculate the MAE and the standard deviation of the MAE for the model's energy predictions. The relative difference (RD), as defined in Eq. 18, is intended to indicate model performance compared to the average level. The results for the baseline model are from our replicated experiments, and SE3Set uses a 3-layer configuration, which corresponds to the results in Table 3. (a) The MAEs of the total energy of the whole molecule. (b) The RD of different models on total energy. (c) The MAEs of the total energy of SE3Set with different numbers of fragments. (d) The MAEs of the energy relative to each atom. (e) The RD of different models on the energy relative to each atom. (f) The MAEs of the energy of SE3Set relative to each atom with different number of fragments.

We compare the MAE of the total energy per molecule and the MAE of the energy relative to each atom separately. For all models, both the MAEs of the total energy and the MAEs averaged to each atom become progressively larger as the size of the molecule increases as shown in Fig. 3 (a) and (d), which shows the interactions, especially the high order interactions are more complicated and significant in larger molecules. However, the MAEs of SE3Set grow significantly slower than the other baseline models. Additionally, the RD curves in Fig. 3 (b) and (e) indicate that SE3Set achieves better performance on large molecules and has the lowest MAEs when the number of atoms interval lower bound is greater than 60. It is also worth noting that the advantage of SE3Set becomes progressively more apparent as the size of the molecule increases, reflected by the decrease in its RD with an increasing number of atoms. These results further support our speculation that SE3Set is more effective compared to other models when learning on larger molecules.

To further analyze the impact of the number of hyperedges on the model performance in addition to the number of nodes (which corresponds to the number of atoms), we also show the results of the variation of MAEs of SE3Set with the number of fragments in Fig. 3 (c) and (f). Since we use the fragmentation method

to construct the hypergraph structure, the number of fragments is associated with the number of hyperedges. The MAEs of the total energy grow larger with the increasing fragment numbers, as more fragments are suggestive of errors accruing from larger molecular systems. When it comes to the MAEs of energy per atom, the increase in MAE with the number of fragments is very slight. This result indicates that our method can handle systems with different fragment numbers more fairly. Considering that molecules with similar atomic numbers may have differences in fragment numbers, this demonstrates that our model is more robust for different molecular structures.

5.4 Ablation studies

To better understand SE3Set, we conduct ablation studies focusing on fragmentation and model architecture. For the explicit overlap fragmentation method, we explore how different fragmentation techniques affect SE3Set's training and compare with the non-overlapping BRICS (Degen et al., 2008; Landrum et al., 2020) strategy on QM9's homo energy task. As Fig. 4 indicates, tests on QM9's homo energy task showed SE3Set's robustness to c_w variations in the fragmentation method. The results show that our method surpasses BRICS, demonstrating the importance of hyperedge interaction. Furthermore, we performed ablation studies on the model architecture. Among two design variants in the E2V attention section, the one using tensor product interactions between nodes and hyperedges proved superior, emphasizing the value of our tensor product-based mechanism and architecture design in enhancing molecular property predictions. Additionally, a 6-layer SE3Set model outperformed its 3-layer counterpart.

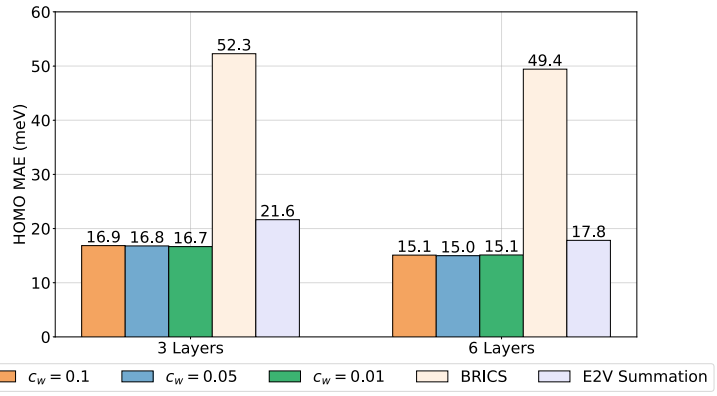

Figure 4: Ablation studies on the QM9 dataset's HOMO task (units: meV). The variable c_w represents the threshold for expansion in the fourth step of fragmentation, guided by the fragment bond order defined in Eq. 19. The term BRICS denotes another fragmentation method implemented in RDKits. Additionally, the E2V summation refers to the architectural framework specified from Eq. 13 to Eq. 15.

Table 4: The MAE for energy (unit: kcal/mol) and forces (unit: kcal/mol $\cdot$ Å) on the AT-AT-CG-CG dataset using 3 layers SE3Set with different cutoff radii (r_c) in the implicit overlap method.

Implicit r_c(Å)	4.0	5.0	6.0
Energy	0.2123	0.1153	0.1103
Force	0.1559	0.1019	0.0937

Unlike the explicit overlap method, the fragment size of the implicit overlap method depends on the choice of r_c. We test the effect of r_c on the model training results on the AT-AT-CG-CG molecule of the MD22 dataset (Table 4). The SE3Set performs better when using higher r_c as it will include more fragments to generate implicit overlaps. The effect of r_c on fragment size is more pronounced for the implicit method than for the explicit method, but it gives good performance for different parameters compared with the baseline models.

6 Conclusion

In conclusion, this study demonstrates the efficacy of SE3Set, a cutting-edge hypergraph neural network architecture, in the realm of molecular representation learning. By meticulously crafting a fragmentation method that coalesces two-dimensional chemical knowledge with three-dimensional spatial information, we establish a robust foundation for constructing hypergraphs that faithfully capture the complex nature of molecular structures. The SE3Set architecture, drawing inspiration from the AllSet framework and the Equiformer, adeptly processes these hypergraphs and preserves the essential invariances and symmetries. SE3Set demonstrates performance comparable to SOTA models in small molecular systems and significantly

outperforms SOTA models in large molecular systems where higher-order many-body interactions are pronounced. The results of our research affirm the potential of SE3Set to model high-order many-body interactions, providing a powerful tool for molecular representation.

7 Impact Statements

This paper advances machine learning techniques for molecular representation, with potential impacts in drug discovery, materials science, and chemical engineering. By improving the modeling of large molecules, our work could enhance drug development, lead to new materials, and improve the understanding of chemical interactions. Additionally, it may aid personalized medicine through better predictions of molecular interactions. We recognize the importance of considering ethical implications, such as data privacy and responsible AI use, and encourage ongoing discussion on these broader impacts.

References

Sameer Agarwal, Jongwoo Lim, Lihi Zelnik-Manor, Pietro Perona, David Kriegman, and Serge Belongie. Beyond pairwise clustering. In 2005 IEEE Computer Society Conference on Computer Vision and Pattern Recognition (CVPR'05), volume 2, pp. 838–845. IEEE, 2005.

Brandon Anderson, Truong Son Hy, and Risi Kondor. Cormorant: Covariant molecular neural networks. Advances in neural information processing systems, 32, 2019.

Sarp Aykent and Tian Xia. Savenet: a scalable vector network for enhanced molecular representation learning. Advances in Neural Information Processing Systems, 36, 2024.

Ilyes Batatia, David P Kovacs, Gregor Simm, Christoph Ortner, and Gábor Csányi. MACE: Higher order equivariant message passing neural networks for fast and accurate force fields. Advances in Neural Information Processing Systems, 35:11423–11436, 2022.

Simon Batzner, Albert Musaelian, Lixin Sun, Mario Geiger, Jonathan P Mailoa, Mordechai Kornbluth, Nicola Molinari, Tess E Smidt, and Boris Kozinsky. E (3)-equivariant graph neural networks for data-efficient and accurate interatomic potentials. Nat. Commun., 13(1):2453, 2022.

Austin R Benson, David F Gleich, and Lek-Heng Lim. The spacey random walk: A stochastic process for higher-order data. SIAM Rev., 59(2):321–345, 2017.

Adam J. Bridgeman and Christopher J Empson. Bond orders between molecular fragments. Chemistry, 12 8: 2252–62, 2006.

He Cao, Zijing Liu, Xingyu Lu, Yuan Yao, and Yu Li. Instructmol: Multi-modal integration for building a versatile and reliable molecular assistant in drug discovery. arXiv preprint arXiv:2311.16208, 2023.

Fangying Chen, Junyoung Park, and Jinkyoo Park. A hypergraph convolutional neural network for molecular properties prediction using functional group. Preprint at `http://arxiv.org/abs/2106.01028`, 2021.

Junwu Chen and Philippe Schwaller. Molecular hypergraph neural networks. Preprint at `http://arxiv.org/abs/2312.13136`, 2023.

Eli Chien, Pan Li, and Olgica Milenkovic. Landing probabilities of random walks for seed-set expansion in hypergraphs. In 2021 IEEE Information Theory Workshop (ITW), pp. 1–6. IEEE, 2021a.

Eli Chien, Chao Pan, Jianhao Peng, and Olgica Milenkovic. You are AllSet: A multiset function framework for hypergraph neural networks. In International Conference on Learning Representations, 2021b.

Stefan Chmiela, Alexandre Tkatchenko, Huziel E Sauceda, Igor Poltavsky, Kristof T Schütt, and Klaus-Robert Müller. Machine learning of accurate energy-conserving molecular force fields. Sci. Adv., 3(5):e1603015, 2017.

Stefan Chmiela, Valentin Vassilev-Galindo, Oliver T Unke, Adil Kabylda, Huziel E Sauceda, Alexandre Tkatchenko, and Klaus-Robert Müller. Accurate global machine learning force fields for molecules with hundreds of atoms. Science Advances, 9(2):eadf0873, 2023.

Michael A Collins and Ryan PA Bettens. Energy-based molecular fragmentation methods. Chem. Rev., 115 (12):5607–5642, 2015.

Benjamin Coors, Alexandru Paul Condurache, and Andreas Geiger. SphereNet: Learning spherical representations for detection and classification in omnidirectional images. In Proceedings of the European conference on computer vision (ECCV), pp. 518–533, 2018.

Shicheng Cui, Qianmu Li, Deqiang Li, Zhichao Lian, Jun Hou, et al. Hyper-mol: Molecular representation learning via fingerprint-based hypergraph. Comput. Intell. Neurosci., 2023, 2023.

Laurianne David, Amol Thakkar, Rocío Mercado, and Ola Engkvist. Molecular representations in AI-driven drug discovery: a review and practical guide. J. Cheminform., 12(1):1–22, 2020.

Jörg Degen, Christof Wegscheid-Gerlach, Andrea Zaliani, and Matthias Rarey. On the art of compiling and using'drug-like'chemical fragment spaces. ChemMedChem: Chemistry Enabling Drug Discovery, 3(10): 1503–1507, 2008.

Kien Do, Truyen Tran, and Svetha Venkatesh. Graph transformation policy network for chemical reaction prediction. In Proceedings of the 25th ACM SIGKDD international conference on knowledge discovery & data mining, pp. 750–760, 2019.

Boxin Du, Changhe Yuan, Robert Barton, Tal Neiman, and Hanghang Tong. Hypergraph pre-training with graph neural networks. Preprint at `http://arxiv.org/abs/2105.10862`, 2021.

Yuanqi Du, Limei Wang, Dieqiao Feng, Guifeng Wang, Shuiwang Ji, Carla P Gomes, Zhi-Ming Ma, et al. A new perspective on building efficient and expressive 3d equivariant graph neural networks. Advances in Neural Information Processing Systems, 36, 2024.

Matthias Fey and Jan Eric Lenssen. Fast graph representation learning with pytorch geometric. Preprint at `http://arxiv.org/abs/1903.02428`, 2019.

Denis Fourches, Eugene Muratov, and Alexander Tropsha. Trust, but verify: on the importance of chemical structure curation in cheminformatics and qsar modeling research. J. Chem. Inf. Model., 50(7):1189, 2010.

Fabian Fuchs, Daniel Worrall, Volker Fischer, and Max Welling. SE (3)-transformers: 3D Roto-translation equivariant attention networks. Advances in Neural Information Processing Systems, 33:1970–1981, 2020.

Johannes Gasteiger, Janek Groß, and Stephan Günnemann. Directional message passing for molecular graphs. In International Conference on Learning Representations, 2019.

Johannes Gasteiger, Shankari Giri, Johannes T Margraf, and Stephan Günnemann. Fast and uncertainty-aware directional message passing for non-equilibrium molecules. Preprint at `http://arxiv.org/abs/2011.14115`, 2020.

Johannes Gasteiger, Florian Becker, and Stephan Günnemann. Gemnet: Universal directional graph neural networks for molecules. Advances in Neural Information Processing Systems, 34:6790–6802, 2021.

Justin Gilmer, Samuel S Schoenholz, Patrick F Riley, Oriol Vinyals, and George E Dahl. Neural message passing for quantum chemistry. In International conference on machine learning, pp. 1263–1272. PMLR, 2017.

Jonathan Godwin, Michael Schaarschmidt, Alexander L Gaunt, Alvaro Sanchez-Gonzalez, Yulia Rubanova, Petar Veličković, James Kirkpatrick, and Peter Battaglia. Simple GNN regularisation for 3D molecular property prediction and beyond. In International Conference on Learning Representations, 2021.

Mark S Gordon, Dmitri G Fedorov, Spencer R Pruitt, and Lyudmila V Slipchenko. Fragmentation methods: A route to accurate calculations on large systems. Chem. Rev., 112(1):632–672, 2012.

Hossein Hajiabolhassan, Zahra Taheri, Ali Hojatnia, and Yavar Taheri Yeganeh. Funqg: Molecular representation learning via quotient graphs. Journal of chemical information and modeling, 63(11):3275–3287, 2023.

Xiaohong Ji, Zhen Wang, Zhifeng Gao, Hang Zheng, Linfeng Zhang, Guolin Ke, et al. Uni-mol2: Exploring molecular pretraining model at scale. arXiv preprint arXiv:2406.14969, 2024.

Hiroshi Kajino. Molecular hypergraph grammar with its application to molecular optimization. In International Conference on Machine Learning, pp. 3183–3191. PMLR, 2019.

Jinwoo Kim, Saeyoon Oh, and Seunghoon Hong. Transformers generalize deepsets and can be extended to graphs & hypergraphs. Advances in Neural Information Processing Systems, 34:28016–28028, 2021.

Jinwoo Kim, Saeyoon Oh, Sungjun Cho, and Seunghoon Hong. Equivariant hypergraph neural networks. In European Conference on Computer Vision, pp. 86–103. Springer, 2022a.

Seojin Kim, Jaehyun Nam, Junsu Kim, Hankook Lee, Sungsoo Ahn, and Jinwoo Shin. Contrastive learning of molecular representation with fragmented views. 2022b.

P-J Kindermans and K-R Müller. Schnet–a deep learning architecture for molecules and materials. J. Chem. Phys., 148(24), 2018.

Arthur Kosmala, Johannes Gasteiger, Nicholas Gao, and Stephan Günnemann. Ewald-based long-range message passing for molecular graphs. In International Conference on Machine Learning (ICML), 2023.

Greg Landrum, Paolo Tosco, Brian Kelley, sriniker, gedeck, NadineSchneider, Riccardo Vianello, Ric, Andrew Dalke, Brian Cole, AlexanderSavelyev, Matt Swain, Samo Turk, Dan N, Alain Vaucher, Eisuke Kawashima, Maciej Wójcikowski, Daniel Probst, guillaume godin, David Cosgrove, Axel Pahl, JP, Francois Berenger, strets123, JLVarjo, Noel O'Boyle, Patrick Fuller, Jan Holst Jensen, Gianluca Sforna, and DoliathGavid. rdkit/rdkit: 2020_03_1 (q1 2020) release, March 2020. URL https://doi.org/10.5281/zenodo.3732262.

Juho Lee, Yoonho Lee, Jungtaek Kim, Adam Kosiorek, Seungjin Choi, and Yee Whye Teh. Set transformer: A framework for attention-based permutation-invariant neural networks. In International conference on machine learning, pp. 3744–3753. PMLR, 2019.

György Lendvay. On the correlation of bond order and bond length. J. Mol. Struct., 501:389–393, 2000.

Biaoshun Li, Mujie Lin, Tiegen Chen, and Ling Wang. Fg-bert: a generalized and self-supervised functional group-based molecular representation learning framework for properties prediction. Briefings in Bioinformatics, 24(6):bbad398, 2023.

Guoyin Li, Liqun Qi, and Gaohang Yu. The Z-eigenvalues of a symmetric tensor and its application to spectral hypergraph theory. Numer. Linear Algebra Appl., 20(6):1001–1029, 2013.

Juncai Li and Xiaofei Jiang. Mol-bert: An effective molecular representation with bert for molecular property prediction. Wireless Communications and Mobile Computing, 2021(1):7181815, 2021.

Yunyang Li, Yusong Wang, Lin Huang, Han Yang, Xinran Wei, Jia Zhang, Tong Wang, Zun Wang, Bin Shao, and Tie-Yan Liu. Long-short-range message-passing: A physics-informed framework to capture non-local interaction for scalable molecular dynamics simulation. In The Twelfth International Conference on Learning Representations, 2024. URL https://openreview.net/forum?id=rvDQtdMnOl.

Yi-Lun Liao and Tess Smidt. Equiformer: Equivariant graph attention transformer for 3D atomistic graphs. In The Eleventh International Conference on Learning Representations, 2022.

Yi-Lun Liao, Brandon Wood, Abhishek Das, and Tess Smidt. EquiformerV2: Improved equivariant transformer for scaling to higher-degree representations. Preprint at http://arxiv.org/abs/2306.12059, 2023.

Kha-Dinh Luong and Ambuj Singh. Fragment-based pretraining and finetuning on molecular graphs. Preprint at http://arxiv.org/abs/2310.03274, 2023.

Jonathan P Mathews and Alan L Chaffee. The molecular representations of coal–a review. Fuel, 96:1–14, 2012.

David L Mobley, Caitlin C Bannan, Andrea Rizzi, Christopher I Bayly, John D Chodera, Victoria T Lim, Nathan M Lim, Kyle A Beauchamp, David R Slochower, Michael R Shirts, et al. Escaping atom types in force fields using direct chemical perception. J. Chem. Theory Comput., 14(11):6076–6092, 2018.

Albert Musaelian, Simon Batzner, Anders Johansson, Lixin Sun, Cameron J Owen, Mordechai Kornbluth, and Boris Kozinsky. Learning local equivariant representations for large-scale atomistic dynamics. Nat. Commun., 14(1):579, 2023.

Eliya Nachmani and Lior Wolf. Molecule property prediction and classification with graph hypernetworks. Preprint at http://arxiv.org/abs/2002.00240, 2020.

Kelly J Pearson and Tan Zhang. On spectral hypergraph theory of the adjacency tensor. Graphs Combin., 30:1233–1248, 2014.

John P Perdew, Kieron Burke, and Matthias Ernzerhof. Generalized gradient approximation made simple. Phys. Rev. Lett., 77(18):3865, 1996.

Raghunathan Ramakrishnan, Pavlo O Dral, Matthias Rupp, and O Anatole Von Lilienfeld. Quantum chemistry structures and properties of 134 kilo molecules. Sci. Data, 1(1):1–7, 2014.

Patrick Reiser, Marlen Neubert, André Eberhard, Luca Torresi, Chen Zhou, Chen Shao, Houssam Metni, Clint van Hoesel, Henrik Schopmans, Timo Sommer, et al. Graph neural networks for materials science and chemistry. Commun. Mater., 3(1):93, 2022.

Lars Ruddigkeit, Ruud Van Deursen, Lorenz C Blum, and Jean-Louis Reymond. Enumeration of 166 billion organic small molecules in the chemical universe database GDB-17. J. Chem. Inf. Model., 52(11):2864–2875, 2012.

T Konstantin Rusch, Michael M Bronstein, and Siddhartha Mishra. A survey on oversmoothing in graph neural networks. Preprint at http://arxiv.org/abs/2303.10993, 2023.

Kristof Schütt, Pieter-Jan Kindermans, Huziel Enoc Sauceda Felix, Stefan Chmiela, Alexandre Tkatchenko, and Klaus-Robert Müller. Schnet: A continuous-filter convolutional neural network for modeling quantum interactions. Advances in neural information processing systems, 30, 2017.

Kristof Schütt, Oliver Unke, and Michael Gastegger. Equivariant message passing for the prediction of tensorial properties and molecular spectra. In International Conference on Machine Learning, pp. 9377–9388. PMLR, 2021.

Annika Stuke, Christian Kunkel, Dorothea Golze, Milica Todorović, Johannes T Margraf, Karsten Reuter, Patrick Rinke, and Harald Oberhofer. Atomic structures and orbital energies of 61,489 crystal-forming organic molecules. Scientific data, 7(1):58, 2020.

Mohammadamin Tavakoli, Alexander Shmakov, Francesco Ceccarelli, and Pierre Baldi. Rxn hypergraph: a hypergraph attention model for chemical reaction representation. Preprint at http://arxiv.org/abs/2201.01196, 2022.

Philipp Thölke and Gianni De Fabritiis. Equivariant transformers for neural network based molecular potentials. In International Conference on Learning Representations, 2021.

Nathaniel Thomas, Tess Smidt, Steven Kearnes, Lusann Yang, Li Li, Kai Kohlhoff, and Patrick Riley. Tensor field networks: Rotation-and translation-equivariant neural networks for 3d point clouds. Preprint at http://arxiv.org/abs/1802.08219, 2018.

Alexandre Tkatchenko, Robert A DiStasio Jr, Roberto Car, and Matthias Scheffler. Accurate and efficient method for many-body van der Waals interactions. Phys. Rev. Lett., 108(23):236402, 2012.

Francesco Tudisco, Austin R Benson, and Konstantin Prokopchik. Nonlinear higher-order label spreading. In Proceedings of the Web Conference 2021, pp. 2402–2413, 2021.

Jeff Wagner, Matt Thompson, David L. Mobley, John Chodera, Caitlin Bannan, Andrea Rizzi, trevorgokey, David L. Dotson, Josh A. Mitchell, jaimergp, Camila, Pavan Behara, Christopher Bayly, JoshHorton, Iván Pulido, Lily Wang, Victoria Lim, Sukanya Sasmal, SimonBoothroyd, Andrew Dalke, Daniel Smith, Brent Westbrook, Josh Horton, Lee-Ping Wang, Richard Gowers, Ziyuan Zhao, Connor Davel, and Yutong Zhao. openforcefield/openff-toolkit: 0.15.1. Testing updates, January 2024. URL `https://doi.org/10.5281/zenodo.10593535`.

Limei Wang, Yi Liu, Yuchao Lin, Haoran Liu, and Shuiwang Ji. ComENet: Towards complete and efficient message passing for 3D molecular graphs. In Alice H. Oh, Alekh Agarwal, Danielle Belgrave, and Kyunghyun Cho (eds.), Advances in Neural Information Processing Systems, 2022.

Yusong Wang, Tong Wang, Shaoning Li, Xinheng He, Mingyu Li, Zun Wang, Nanning Zheng, Bin Shao, and Tie-Yan Liu. Enhancing geometric representations for molecules with equivariant vector-scalar interactive message passing. Nat. Commun., 15(1):313, 2024.

Zun Wang, Guoqing Liu, Yichi Zhou, Tong Wang, and Bin Shao. Efficiently incorporating quintuple interactions into geometric deep learning force fields. In Thirty-seventh Conference on Neural Information Processing Systems, 2023.

Daniel S Wigh, Jonathan M Goodman, and Alexei A Lapkin. A review of molecular representation in the age of machine learning. Wiley Interdiscip. Rev. Comput. Mol. Sci., 12(5):e1603, 2022.

Zhenxing Wu, Jike Wang, Hongyan Du, Dejun Jiang, Yu Kang, Dan Li, Peichen Pan, Yafeng Deng, Dongsheng Cao, Chang-Yu Hsieh, et al. Chemistry-intuitive explanation of graph neural networks for molecular property prediction with substructure masking. Nature Communications, 14(1):2585, 2023.

Zonghan Wu, Shirui Pan, Fengwen Chen, Guodong Long, Chengqi Zhang, and S Yu Philip. A comprehensive survey on graph neural networks. IEEE Trans. Neural. Netw. Learn. Syst., 32(1):4–24, 2020.

Jiacheng Xiong, Zhaoping Xiong, Kaixian Chen, Hualiang Jiang, and Mingyue Zheng. Graph neural networks for automated de novo drug design. Drug Discov. Today, 26(6):1382–1393, 2021.

Manzil Zaheer, Satwik Kottur, Siamak Ravanbakhsh, Barnabas Poczos, Russ R Salakhutdinov, and Alexander J Smola. Deep sets. Advances in neural information processing systems, 30, 2017.

Dengyong Zhou, Jiayuan Huang, and Bernhard Schölkopf. Learning with hypergraphs: Clustering, classification, and embedding. Advances in neural information processing systems, 19, 2006.

Gengmo Zhou, Zhifeng Gao, Qiankun Ding, Hang Zheng, Hongteng Xu, Zhewei Wei, Linfeng Zhang, and Guolin Ke. Uni-mol: A universal 3d molecular representation learning framework. In International Conference on Learning Representations, 2023.

Jie Zhou, Ganqu Cui, Shengding Hu, Zhengyan Zhang, Cheng Yang, Zhiyuan Liu, Lifeng Wang, Changcheng Li, and Maosong Sun. Graph neural networks: A review of methods and applications. AI open, 1:57–81, 2020.

A Details of fragmentation steps

Before delving deeper into the specifics of our fragmentation method, it's important to establish a foundational understanding through key definitions and concepts. We first give the definition of bond order here,

Definition A.1. The bond order represents the multiplicity or the number of shared electron pairs that constitute a covalent bond between two atoms.

The bond order matrix $\mathbf{B}$ is an $N \times N$ representation of bond strength between atoms in a molecule, with higher bond order values indicating stronger bonds. This symmetric matrix ($B_{ij} = B_{ji}$) is crucial for studying the molecular structure and reactivity, capturing bond nuances including delocalized and resonance bonds in computational chemistry.

Based on the design principles in Sec. 4.1, the detailed step-by-step methodology of explicit overlap fragmentation method is shown as follows,

1. The pre-processing step begins by analyzing the given molecule through its bond order matrix, denoted as B. Identify and mask bonds that are part of functional groups or rings, as well as those with a bond order of $B_{ij} \geqslant 2$. Functional groups are then identified using predefined SMARTS patterns for accurate matching. To achieve a more generalized representation of functional groups, topologically adjacent functional groups are merged into a single entity. This aggregation allows to focus on specific subfunctional groups that are of particular interest, simplifying the complexity of the molecular structure for subsequent analysis.

2. Following the masking of selected bonds, the Breadth-First Search (BFS) algorithm is employed to reconstruct the substructures, denoted as $\{\mathfrak{S}\}$, from the remaining unmasked bonds. These groups represent the core structural units of the molecule as discussed at the outset of this section.

3. Consolidate the previously identified groups $\{\mathfrak{S}\}$ into larger molecular fragments, applying a set of predefined rules to guide the merging process. These rules are meticulously designed to ensure that each resulting fragment, now denoted as $\{\mathfrak{F}\}$, contains at least a minimum specified number of atoms. For a comprehensive understanding of the merging criteria, one can refer to the detailed rules outlined in C.

4. Extend each fragment $\{\mathfrak{F}\}$ by incorporating adjacent groups from $\{\mathfrak{S}\}$ to enrich the connectivity between molecular fragments, thus intentionally creating regions of overlap among the fragments. This expansion is controlled by a cutoff threshold, denoted as c_w, which is typically a function based on interatomic distances. The fragment bond order (Lendvay, 2000; Bridgeman & Empson, 2006), symbolized by W_{fs}, is used to quantitatively assess the interaction strength between a fragment $\mathfrak{F}_i$ and an adjacent substructure $\mathfrak{S}_j$. This method reflects the interaction strength based on the proximity of atoms in different fragments, expressed by the following equation:

$$W_{fs} = \sum_{i \in \mathfrak{F}_f, j \in \mathfrak{S}_s} \exp\left(-\frac{(d_{ij} - d_{ij}^e) \cdot d_{ij}^e}{(0.25\ \text{Å})^2}\right), \tag{19}$$

   where d_{ij} represents the interatomic distance between atoms i and j, and d_{ij}^e stands for the equilibrium distance typically expected for such a bond. This equation is utilized to determine which substructures should be included in the expansion of a fragment, based on the strength of their interactions as governed by the distance function. Additionally, in alignment with Pauling's concept of "chemist's bond order" (Lendvay, 2000), an alternative method is introduced to calculate the bond order using a single exponential function,

$$W_{fs} = \sum_{i \in \mathfrak{F}_f, j \in \mathfrak{S}_s} \exp\left(-(d_{ij} - d_{ij}^e)\right), \tag{20}$$

   where W_{fs} encapsulates the bond order between atoms belonging to a fragment $\mathfrak{F}_f$ and a substructure $\mathfrak{S}_s$. In this context, d_{ij} signifies the actual measured distance between atom i and atom j. The term

d_{ij}^e refers to the theoretical equilibrium covalent bond length, which is estimated by summing the empirical covalent radii of the two atoms involved, given by:

$$d_{ij}^e = r_{z_i} + r_{z_j}, \tag{21}$$

where r_{z_i} is the empirical covalent radius of an atom with atomic number z_i. This function provides a simplified yet effective representation of bond order, allowing us to gauge the bonding interactions within the molecular structure concerning the proximity of the atoms.

The implicit overlap fragmentation method only changes the step 4, the details of the changed fourth step have been spelled out in 4.1.

B Functional groups SMARTS

In the initial phase of our fragmentation approach, we identify functional groups using the SMARTS pattern-matching language. In Table 5, we present the complete list of SMARTS patterns utilized, which have been expanded upon from the default set found within the Open Force Field toolkit (Mobley et al., 2018; Wagner et al., 2024) (accessible at: `https://github.com/openforcefield/openff-fragmenter/blob/main/openff/fragmenter/data/default-functional-groups.json`).

Table 5: SMARTS patterns for functional groups employed in the preprocessing stage of fragmentation.

Functional Groups Name	SMARTS
hydrazine	[NX3:1][NX3:2]
hydrazone	[NX3:1][NX2:2]
nitric oxide	[N:1]-[O:2]
amide	[#7:1][#6:2](=[#8:3]), [NX3:1][CX3:2](=[OX1:3])[NX3:4]
amide negative ion	[#7:1][#6:2](-[O-:3])
aldehyde	[CX3H1:1](=[O:2])[#6:3]
sulfoxide	[#16X3:1]=[OX1:2], [#16X3+:1][OX1-:2]
sulfonyl	[#16X4:1](=[OX1:2])=[OX1:3]
sulfinic acid	[#16X3:1](=[OX1:2])[OX2H,OX1H0-:3]
sulfonic acid	[#16X4:1](=[OX1:2])(=[OX1:3])[OX2H,OX1H0-:4]
sulfinamide	[#16X4:1](=[OX1:2])(=[OX1:3])([NX3R0:4])
phosphine oxide	[PX4:1](=[OX1:2])([#6:3])([#6:4])([#6:5])
phosphonate	[P:1](=[OX1:2])([OX2H,OX1-:3])([OX2H,OX1-:4])
phosphate	[PX4:1](=[OX1:2])([#8:3])([#8:4])([#8:5])
carboxylic acid	[CX3:1](=[O:2])[OX1H0-,OX2H1:3]
nitro	[NX3+:1](=[O:2])[O-:3], [NX3:1](=[O:2])=[O:3]
ester	[CX3:1](=[O:2])[OX2H0:3]
tri-halide	[#6:1]([F,Cl,I,Br:2])([F,Cl,I,Br:3])([F,Cl,I,Br:4])
hydroxyl	[#8:1]-[#1:2]

C Merge process of fragmentation

During the third step of our fragmentation method, we introduce a strategy to enlarge substructures, ensuring that each initial fragment contains at least $n_{\min}$ atoms, with $n_{\min}$ being a predefined integer. To maintain permutation invariance for a molecule, we incorporate weights, W_{fs}, to guide the sequence of merging. The process is outlined in the pseudocode (Algorithm 1). The calculation of W is based on either Eq. 19 or Eq. 20. By considering the sum of bond orders to other groups, we assess each group's centrality. The groups are then ordered first by the number of atoms they contain, followed by the summation of their bond orders, ensuring that the fragmentation merge process is permutation invariant when following this specified sequence. The algorithm then assists smaller groups in merging with others to achieve a size of at least $n_{\min}$ atoms.

Algorithm 1 Pseudo code of fragmentation merge step.

Input: groups $\{\mathfrak{G}\}$, minimum atoms number $n_{\min}$, maximum atoms number $n_{\max}$, Topological bond order matrix B, isolated threshold c_{is}
$m = |\{\mathfrak{G}\}|$
Isolate groups $\{\mathfrak{G}^{\mathfrak{I}}\} = \{\}$
Calculate fragmentation bond order matrix $W_{\mathfrak{G}_i\mathfrak{G}_j}$.
Sort $\{\mathfrak{G}\}$ in descending order based on the following attributes: number of atoms, $\sum_{\mathfrak{G}',\mathfrak{G}'\neq\mathfrak{G}} W_{\mathfrak{G}\mathfrak{G}'}$.
repeat
  Pop last fragment as $\mathfrak{G}_k$ from $\{\mathfrak{G}\}$
  for $i = m-1$ **to** 1 **do**
    $a = \text{MAX\_INT}, merge\_idx = -1$
    if any $B_{ij} \geqslant 1, i \in \mathfrak{G}_i j \in \mathfrak{G}_k$ **and** $|\mathfrak{G}_i| < a$ **and** $a + |\mathfrak{G}_i| \leqslant n_{\max}$ **then**
      $a = |\mathfrak{G}_i|, merge\_idx = i$
    end if
  end for
  if $merge\_idx == -1$ **then**
    for $i = m-1$ **to** 1 **do**
      if any $W_{\mathfrak{G}_i\mathfrak{G}_k} \geqslant c_{is}$ **and** $|\mathfrak{G}_i| < a$ **then**
        $a = |\mathfrak{G}_i|, merge\_idx = -1$
      end if
    end for
  end if
  if $merge\_idx \neq -1$ **then**
    Merge $\mathfrak{G}_k$ to $\mathfrak{G}_{merge\_idx}$
    Resort $\{\mathfrak{G}\}$ by the same priority and update W.
  else
    Add $\{\mathfrak{G}_k\}$ to $\{\mathfrak{G}^{\mathfrak{I}}\}$
  end if
until $|\{\mathfrak{G}_k\}| \geqslant n_{\min}$
$\{\mathfrak{F}\} = \{\mathfrak{G}\} \cup \{\mathfrak{G}^{\mathfrak{I}}\}$

Initially, we consider topologically adjacent groups with the fewest atoms. If a target group lacks topological neighbors, we proceed to merge based on the bond order from W. We introduce a threshold c_{is} that allows a group to remain isolated if it is significantly distant from others. It should be noted that isolated groups may not meet the minimum atom number requirement; however, they could be further expanded in the subsequent fragmentation step, depending on the chosen thresholds for c_{is} and c_w (refer to Sec. 4.1). Overall, this algorithm ensures a permutation-invariant merging process.

D Distribution of fragmentation dataset

Different parameters used in the fragmentation process can lead to a variety of hyperedges, which in turn result in distinct hypergraphs utilized for training our model. To illustrate the variances attributed to different fragmentation parameters or methods (such as BRICS implemented in RDKit (Degen et al., 2008; Landrum et al., 2020)), we use the QM9 dataset (Ruddigkeit et al., 2012; Ramakrishnan et al., 2014) to demonstrate how the data distributions attached to hypergraphs may change.

The impact of adjusting fragmentation parameters on the composition of hyperedges can be observed in Fig. 5. Altering the expansion threshold c_w within a certain range has a minimal effect on fragment expansion. However, when utilizing the Lendvay bond order (Eq. 19), fragments tend to comprise fewer atoms compared to when using the Exponential bond order (Eq. 20). This difference is likely due to the more gradual decline in the exponential function, which results in a greater cumulative contribution to the weights W_{fs}.

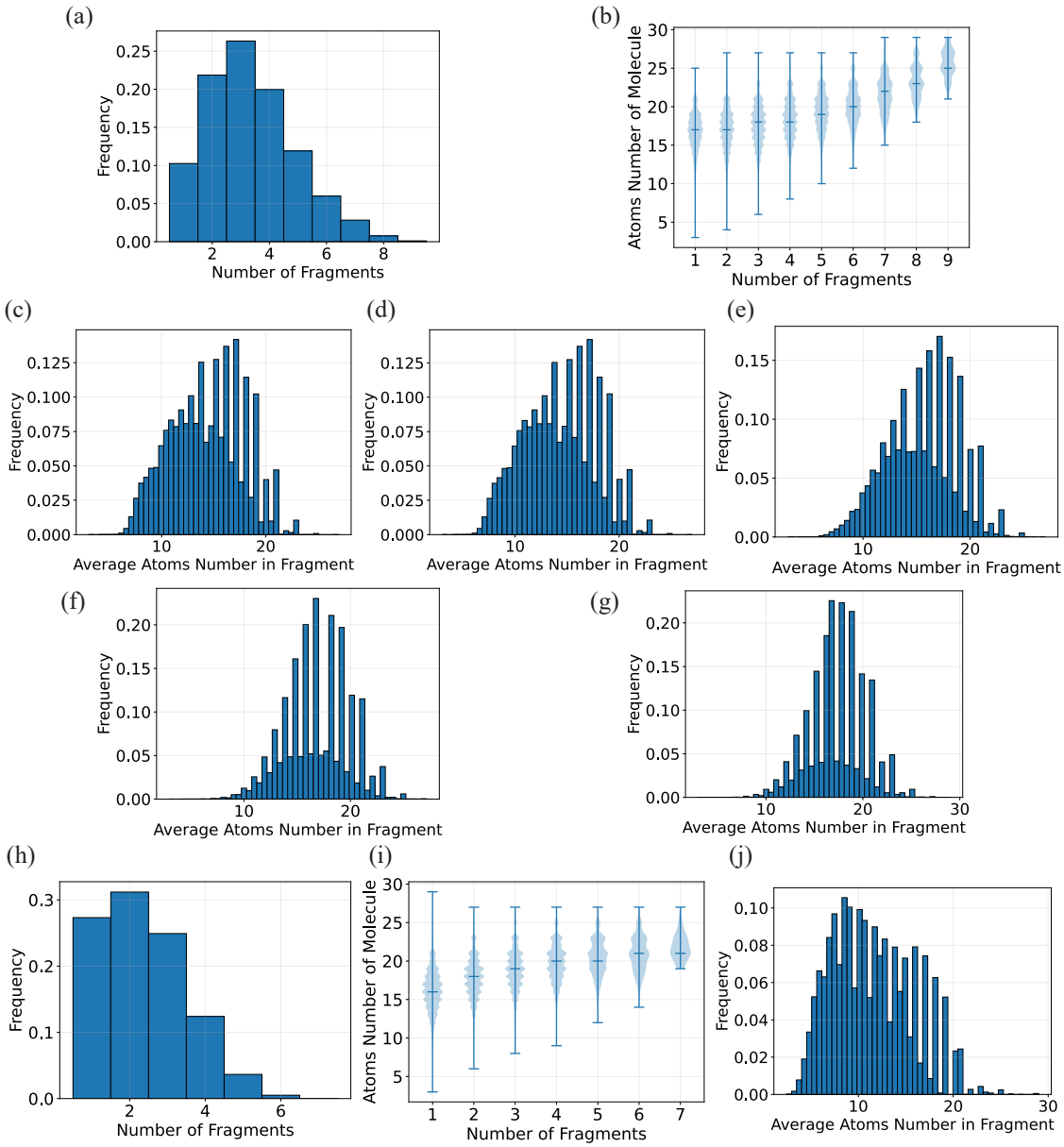

Figure 5: Distribution of fragments in QM9 dataset. (a) Fragment Count Distribution. The distribution remains consistent regardless of the value of c_w or the bond order calculation method employed. (b) Molecule Size vs. Fragment Count Distribution. Generally, the more atoms a molecule has, the more fragments will generate. It is also invariant for c_w or bond order calculation scheme. Average Atom Count per Fragment Distribution (c) $c_w = 0.1$, (d) $c_w = 0.05$, (e) $c_w = 0.01$ for Lendvay bond order and (f) $c_w = 0.4$ and (g) $c_w = 0.2$ for exponential bond order, respectively. (h) BRICS Fragment Count Distribution. (i) BRICS Molecule Size vs. Fragment Count Distribution (j) BRICS Average Atom Count per Fragment.

Our ablation study (Sec. 5.4) also includes a comparison with the BRICS fragmentation method. Fragments generated by the BRICS method are observed to contain significantly fewer atoms since this approach does not create overlapping regions between different fragments.

E Proof of SE(3) equivariance

The SE3Set consists of the basic modules including linear, depth-wise tensor product, gate activation, and layer normalization. Here we will prove the SE3 equivariance for these modules. As the inputs of SE3Set are all invariant to translation in 3D Euclidean space, we only need to prove the $SO(3)$ equivariance.

Let $g \in SO(3)$ and the $\mathcal{D}$ denote the group representation of $SO(3)$. Besides, we denote the irreps feature as $\mathbf{f}$, and $\mathbf{f}^l$ denotes the k^{th} feature vector in irreducible representations space of $SO(3)$ with l order.

Linear Linear module deploys separated linear operations for each l in the irreps feature. For each l, we consider the output channel $\mathbf{f}_k^l$. Then we have

$$\mathbf{f}_j^l = \text{Linear}(\mathbf{f}^l) = \sum_k w_{kj}^l \mathbf{f}_k^l \tag{22}$$

where w_{kj}^l denotes the linear combination weight. When acting $\mathcal{D}(g)$ at the input f^l, we can find that

$$\begin{aligned}
(\mathbf{f}_j^l)' &= \text{Linear}(\mathcal{D}(g)\mathbf{f}^l) && (23)\\
&= \sum_k w_{kj}^l \mathcal{D}(g)\mathbf{f}_k^l && (24)\\
&= \mathcal{D}(g) \sum_k w_{kj}^l \mathbf{f}_k^l && (25)\\
&= \mathcal{D}(g)\mathbf{f}_j^l && (26)
\end{aligned}$$

Therefore, the linear module is $SO(3)$ equivariant.

Depth-wise Tensor-product Tensor product is an equivariant operation for $\mathcal{D}(g)$

$$\mathcal{D}(g)(\mathbf{f}_{k_1}^l \otimes \mathbf{f}_{k_2}^l) = (\mathcal{D}(g)\mathbf{f}_{k_1}^l) \otimes (\mathcal{D}(g)\mathbf{f}_{k_2}^l) \tag{27}$$

The depth-wise tensor product differs from the tensor product only in that one order l vector in output irreps feature depends only on one order l' feature, where l' is equal to or different from l. Hence the $SO(3)$ equivariance still holds for depth-wise tensor product.

Gate As the $l = 0$ vector is invariant for $\mathcal{D}(g)$, we have

$$\begin{aligned}
\text{Gate}(\mathcal{D}(g)\mathbf{f}_k^0) &= \text{Activation}(\mathcal{D}(g)\mathbf{f}_k^0) && (28)\\
&= \text{Activation}(\mathbf{f}_k^0) && (29)\\
&= \mathcal{D}(g)\text{Activation}(\mathbf{f}_k^0) && (30)\\
&= \mathcal{D}(g)\text{Gate}(\mathbf{f}_k^0) && (31)
\end{aligned}$$

We use the non-linear output from the $\text{Activation}(\mathcal{D}(g)\mathbf{f}_{k_1}^0)$ (i.e. Sigmoid in SE3Set) as the weight which multiplies $l > 0$ vector to implement the gate function. Thus for $l > 0$, we also have

$$\begin{aligned}
\text{Gate}(\mathcal{D}(g)\mathbf{f}_{k_1}^l) &= \text{Activation}(\mathcal{D}(g)\mathbf{f}_{k'}^0)\mathcal{D}(g)\mathbf{f}_{k_1}^l && (32)\\
&= \text{Activation}(\mathbf{f}_{k_1}^0)\mathcal{D}(g)\mathbf{f}_{k_1}^l && (33)\\
&= \mathcal{D}(g)\text{Gate}(\mathbf{f}_{k_1}^l) && (34)
\end{aligned}$$

So the gate function is $SO(3)$ equivariant for all l vectors.

Layer Normalization For $l = 0$, as it is $SO(3)$ invariant, the general layer normalization is adapted

$$\text{LN}(\mathbf{f}_k^0) = \left(\frac{\mathbf{f}_k^0 - \mu}{\text{RMS}_C(\|\mathbf{f}^0\|)}\right)\gamma + \beta \tag{35}$$

where C denotes the channel number corresponding and $\|\cdot\|$ denotes the 2-norm for each channel vector. μ is the mean value of $\mathbf{f}^0$. Learnable weight γ and learnable bias β are also deployed. The module is $SO(3)$ invariant as $\mathbf{f}_k^0$ is $SO(3)$ invariant. The layer normalization for $l > 0$ vector has the following form

$$\mathrm{LN}(\mathbf{f}_k^l) = \left(\frac{\mathbf{f}_k^l}{\mathrm{RMS}_C(\|\mathbf{f}^l\|)}\right)\gamma \tag{36}$$

We can prove the module is $SO(3)$ equivariant as

$$\mathrm{LN}(\mathcal{D}(g)\mathbf{f}_k^l) = \left(\frac{\mathcal{D}(g)\mathbf{f}_k^l}{\mathrm{RMS}_C(\|\mathcal{D}(g)\mathbf{f}^l\|)}\right)\gamma \tag{37}$$

$$= \left(\frac{\mathcal{D}(g)\mathbf{f}_k^l}{\mathrm{RMS}_C(\|\mathbf{f}^l\|)}\right)\gamma \tag{38}$$

$$= \mathcal{D}(g)\mathrm{LN}(\mathbf{f}_k^l) \tag{39}$$

F Concepts of irreps features and tensor product

Irreps features The SE3Set model utilizes the special orthogonal group SO(3) to capture three-dimensional rotational symmetries in molecular structures. This approach is similar to Equiformer (Liao & Smidt, 2022; Liao et al., 2023). It employs irreducible representations (irreps) of SO(3), parameterized by an integer l, which correspond to spherical harmonics (SH) functions Y_l^m. These functions imbue feature vectors with rotational information, ensuring the model's equivariance to rotations and enabling consistent geometric property analysis. This approach is key to the model's ability to accurately represent and predict molecular and other rotationally invariant systems.

Tensor product To boost the model's expressive power, we consider interactions between irrep features of different angular momenta l through the tensor product, which merges two irreps l_1 and l_2 into a new irrep with angular momentum l_3. This is achieved using Clebsch-Gordan coefficients in an expansion weighted by w_{m_1,m_2}.

$$\begin{aligned} f_{m_3}^{l_3} &= (f_{m_1}^{l_1} \otimes f_{m_2}^{l_2})_{m_3} \\ &= \sum_{m_1,m_2} w_{m_1,m_2} C_{l_1,m_1,\ l_2,m_2}^{l_3,m_3} f_{m_1}^{l_1} f_{m_2}^{l_2}. \end{aligned} \tag{40}$$

To reduce complexity, a depth-wise tensor product $\otimes^{\mathrm{DTP}}$ is adopted from the Equiformer (Liao & Smidt, 2022; Liao et al., 2023), utilizing internal weights to streamline computations. Input-dependent tensor product weights are denoted as $\otimes_w^{\mathrm{DTP}}$, ensuring computational efficiency while preserving equivariance for feature interactions.

G Results of MD17

The MD17 dataset (Chmiela et al., 2017) features a wide variety of molecular configurations simulated at 500 K, with high-resolution trajectories and labeled with energies and forces from the PBE+vdW-TS method (Perdew et al., 1996; Tkatchenko et al., 2012). SE3Set's performance on this dataset is shown in Table 6. SE3Set outperforms Equiformer in accuracy, highlighting its refined force calculation capabilities. In small molecular systems, higher-order many-body interactions are less pronounced, and as a result, SE3Set does not significantly outperform other state-of-the-art (SOTA) models.

H Complexity Analysis

The computational complexity mainly depends on the V2E module and the E2V module.

The V2E module aggregates the information from each atom in one fragment to generate atom-wise hyperedge features. Considering the system is split into m fragments and each fragment has n_i atoms, this module

Table 6: A comparison of Mean Absolute Errors (MAEs) across various benchmarked models. SE3Set is trained on the MD17 dataset with a configuration of 950 training samples and 50 validation samples. Bolding shows the best model and underlining shows the second best model and the underlining tilde shows third best model. The MAEs reflect the precision of energy predictions in units of kcal/mol and forces in units of kcal/(mol·Å). The results of each baseline come from the corresponding articles (Schütt et al., 2017; Gasteiger et al., 2019; Schütt et al., 2021; Thölke & De Fabritiis, 2021; Gasteiger et al., 2021; Batzner et al., 2022; Wang et al., 2024; Liao & Smidt, 2022; Wang et al., 2023).

		SchNet	DimeNet	PaiNN	ET	GemNet	NequIP (l=3)	ViSNet	QuinNet	Equiformer	SE3Set
Aspirin	Energy	0.37	0.204	0.167	0.123	-	0.131	**0.116**	0.119	0.122	0.130
	Force	1.35	0.499	0.338	0.253	0.217	0.184	0.155	**0.145**	0.152	0.153
Ethanol	Energy	0.08	0.064	0.064	0.052	-	0.051	0.051	**0.050**	0.051	0.054
	Force	0.39	0.230	0.224	0.109	0.085	0.071	**0.060**	**0.060**	0.067	0.062
Malonaldehyde	Energy	0.13	0.104	0.091	0.077	-	0.076	0.075	0.078	**0.074**	**0.074**
	Force	0.66	0.383	0.319	0.169	0.155	0.129	0.100	**0.097**	0.125	0.103
Naphthalene	Energy	0.16	0.122	0.116	0.085	-	0.113	**0.085**	0.101	**0.085**	0.113
	Force	0.58	0.215	0.077	0.061	0.051	**0.039**	**0.039**	**0.039**	0.046	**0.039**
Salicylic acid	Energy	0.20	0.134	0.116	0.093	-	0.106	**0.092**	0.101	0.099	0.108
	Force	0.85	0.374	0.195	0.129	0.125	0.090	0.084	**0.080**	0.090	0.090
Toluene	Energy	0.12	0.102	0.095	0.074	-	0.092	**0.074**	0.080	0.085	0.093
	Force	0.57	0.216	0.094	0.067	0.060	0.046	**0.039**	**0.039**	0.048	0.046
Uracil	Energy	0.14	0.115	0.106	0.095	-	0.104	**0.095**	0.096	0.099	0.103
	Force	0.56	0.301	0.139	0.095	0.097	0.076	**0.062**	**0.062**	0.076	0.067

includes $\sum_i^m n_i(n_i-1)$ pair-wise messages for the attention architecture. Actually, this number depends on the fragment hyperparameter n_{min} and n_{max}, in particular for the explicit overlap method, also on c_w. For the explicit overlap method, this module would have higher complexity than the implicit overlap method because the explicit overlap has a higher average number of atoms in each fragment.

For each atom, the E2V module aggregates all the hyperedge features that an atom possesses. Thus the calculated pair-wise message number depends on the number of fragments per atom shared, corresponding to the introduced overlap degrees. Then the computational complexity of the explicit overlap method in this module depends on the c_w for the explicit overlap method and r_c for the implicit overlap method.

To give a general approximate complexity, we consider a system with N atoms. When using the explicit overlap method, if the system has m fragments with an average n_{exp} atoms in one fragment, the V2E module's complexity will be $O(mn_{\text{exp}}^2)$ according to the previous analysis. For the E2V module, the number of fragments to which each atom belongs on average can be represented as mn_{exp}/N. Thus, the complexity will be $O(mn_{\text{exp}})$ when considering N atoms.

Similarly, for the implicit overlap method, the complexity of the V2E module will be $O(n_{\mathcal{F}}n_{\text{imp}}N)$, where $n_{\mathcal{F}}$ represents the average number of neighbor fragments within cutoff per atom and n_{imp} denotes the average atoms in one fragment. And the complexity of the E2V module is $O(n_{\mathcal{F}}N)$.

Compared to the explicit overlap method, the implicit overlap method has lower computational complexity. As we can approximate that $n_{\mathcal{F}}n_{\text{imp}} \approx n_{\text{exp}}$ (overlap degree is similar) and determine $mn_{\text{imp}} = N$ (implicit overlap method has same fragment number m but without extra count of atoms in n_{imp}). On the other hand, we can determine $mn_{\text{exp}} \geqslant N$ as the explicit overlap will count atoms more times. Hence the explicit overlap method has higher complexity than the implicit overlap on the V2E Module according to the deduction below

$$mn_{\text{exp}}^2 \geqslant Nn_{\text{exp}} \approx n_{\mathcal{F}}n_{\text{imp}}N \tag{41}$$

$$mn_{\text{exp}} \approx mn_{\mathcal{F}}n_{\text{imp}} \approx n_{\mathcal{F}}N \tag{42}$$

To better support the analysis, we have tested the inference speed of SE3Set on part of QM9 and MD22 datasets as shown in Table 7. Larger fragments, with smaller c_w, reduce speed, more so in larger molecules. Speed drops with increased fragment size (smaller c_w or larger r_c), and the explicit overlap method is slower than the implicit, leading to our preference for the latter in MD22. This highlights the need to optimize

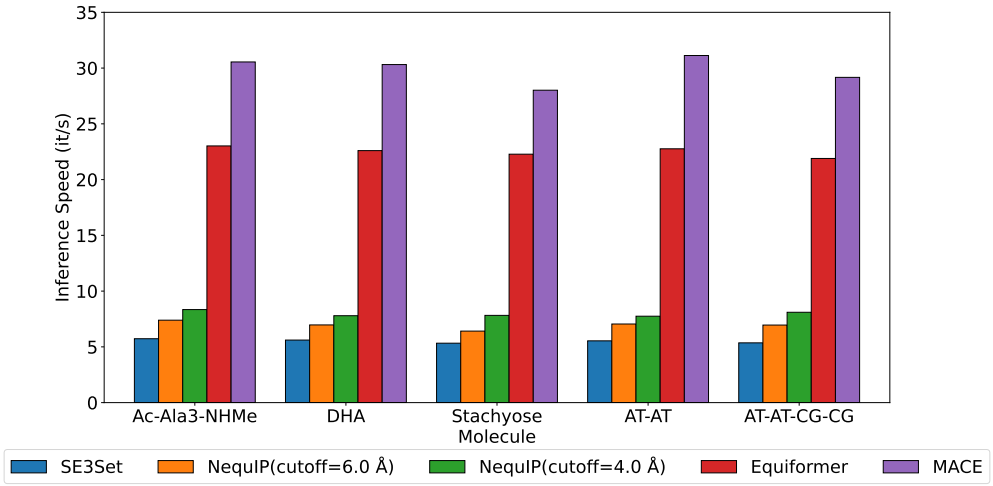

Figure 6: Inference speeds of different models on the MD22 dataset in units iteration/s. The average inference speeds were calculated for each molecule dataset. All tests were performed on a single Tesla A100 80G. The SE3Set includes 3 layers and a different cutoff is set (4 Åand 6 Å) for NeuqIP. The other models. The other models use parameter configurations that correspond to the results reported in their respective studies.

fragment size for a trade-off between detailed interaction capture and speed, particularly in big molecular systems. Additionally, the explicit overlap method is slower than the implicit overlap method, which confirms our previous analysis.

Table 7: The inference speed (unit: iterations/s) of SE3Set with different c_w or r_c. The tests on the MD22 dataset only use the AT-AT-CG-CG subset.

	dataset	Explicit c_w			Implicit r_c		
		0.1	0.05	0.01	4.0	5.0	6.0
Inference speed	QM9	11.60	11.54	11.37	-	-	-
	MD22 (AT-AT-CG-CG)	2.62	2.29	1.68	2.92	2.90	2.87

Moreover, we have evaluated the inference time with different baseline models. The results in Fig. 6 show SE3Set runs slightly slower than the other models. This is reasonable as we have included more pairwise node information in our hypergraph. The improvement in our model's performance indicates that our model requires further optimization to achieve a better balance between efficiency and performance.

The number of parameters of SE3Set and other baseline models are showed in Fig. 8. SE3Set achieves better performance using fewer parameters.

Table 8: Number of parameters with different models.

Model	ViSNet	QuinNet	SE3Set(6 Layers)	SE3Set(3 Layers)
No. of Parameters (Million)	10	9	6.3	3.5

I Training details

This section outlines the training specifics, encompassing the fragmentation parameters, SE3Set hyperparameters, and certain implementation nuances utilized in our experimental setup.

Our dataset construction is founded on PyTorch Geometric (Fey & Lenssen, 2019) augmented with our fragmentation process (Sec. 4.1). Due to inconsistencies in molecular topology identified through RDKit's sanitization routine (Landrum et al., 2020), 1,403 data points were excised from the original dataset. We designated 110,000 data points for the training set and 10,000 for the validation set, selected at random.

We used an explicit overlap scheme on the QM9 and MD17 datasets because of their relatively small molecular systems. We implemented two distinct schemes for calculating fragment bond orders, following either Eq. 19 or Eq. 20. The parameters for fragmentation are detailed below. Given that the MD17 molecules are relatively small, the merge step in the fragmentation process was not actually utilized. However, we present the fragmentation parameters here for the sake of completeness.

Besides, we adopt an implicit overlap scheme on the MD22 dataset and OE62 dataset to reduce computational resource consumption. The details of cutoff r_c introduced in 4* can be found in Table 11.

On the QM9 and MD17 datasets, our model was trained using a single Tesla V100 GPU with 32GB of memory, except for the 6-layer model employing the exponential bond order on the QM9 dataset, which was trained on two Tesla V100 GPUs with 32GB each. For MD22 dataset and OE62 dataset, our model was trained on a single Tesla A100 GPU with 80GB of memory.

We selected $l = 2$ for our irreducible representations (irreps) feature, which includes both node and hypergraph features. For the radial basis function (RBF), we utilized Gaussian basis functions or Bessel basis functions for the QM9 dataset (Ruddigkeit et al., 2012; Ramakrishnan et al., 2014) and exponential basis functions for the MD17 dataset, MD22 dataset and OE62 dataset (Chmiela et al., 2017). Details can be found in Table 9 and Table 10.

Table 9: Hyper-parameters for training SE3Set model. In the context of hyperparameter settings for dimensions, the symbols e and o are used to denote even and odd parity, respectively.

	QM9	MD17	MD22	OE62
Hyper-parameters	Value or descriptions	Value or descriptions	Value or descriptions	Value or discriptions
Optimizer $n_{\min}$	AdamW	AdamW	AdamW	AdamW
Learning rate scheduler	Cosine	Cosine	Cosine	Cosine
Warm up epochs $n_{\max}$	5	10	10	10
Minimum learning rate	1.0×10^{-6}	1.0×10^{-6}	1.0×10^{-6}	1.0×10^{-6}
Batch size	$32, 128$	8	8	32
Number of epochs	400	1500	1500	400
Weight decay	5.0×10^{-3}	1.0×10^{-6}	1.0×10^{-6}	1.0×10^{-6}
Dropout rate	0.1	0.0	0.0	0.0
RBF cutoff (Å)	42.0	Max distance of used atom pairs		
Basis Type	Gaussian or Bessel	Exponential	Exponential	Exponential
Number of Basis	128 or 8	32	32	32
Number of Blocks	3 or 6	3 or 6	6	3
Node embedding dimension		[(128, 0e), (64, 1o), (32, 2e)]		
Hyperedge embedding dimension		[(128, 0e), (64, 1o), (32, 2e)]		
Attention head dimension		[(32, 0e), (16, 1o), (8, 2e)]		
Feed forward dimension		[(384, 0e), (192, 1o), (96, 2e)]		
Output feature dimension		[(512, 0e)]		

Table 10: Hyper-parameters for fragmentation. The expanded threshold does not work for models training on the MD22 dataset because they adapt implicit overlap scheme.

Bond Order Methods	Bond Order by Lendvay (19)	Fragmentation by Exponential (20)
minimum atoms number $n_{\min}$	2	2
maximum atoms number $n_{\max}$	6	6
isolated threshold (c_{is})	0.1	0.4
expand threshold (c_w)	0.1	0.2, 0.4

Table 11: Hyper-parameters for step 4* of implicit overlap scheme in MD22 and OE62 experiments.

Dataset	MD22					OE62
	Ac-Ala3-NHMe	DHA	Stachyose	AT-AT	AT-AT-CG-CG	
distance cutoff r_c (Å)	5.0	4.0	4.0	6.0	6.0	5.0

Table 12: Performance comparing with some pre-trained models on 3 tasks (HOMO, LUMO, GAP) of QM9 dataset. We use the average mean absolute error performance here following the article of baselines. All the baseline results are extracted from the origin articles (Zhou et al., 2023; Ji et al., 2024; Cao et al., 2023).

Model	UniMol	UniMol-2	InstructMol	SE3Set
Avg. MAE (meV)	127	95	136	19

J Comparison with pre-trained baselines

Pre-trained model has become more popular in molecular representation learning recently. For completeness, we have added the performance comparison with some state-of-the-art pre-trained models in this section. We choose the reported average MAE on 3 targets (HOMO, LUMO, gap) of QM9 as a metric, our model performs better than those pre-trained models on this metric as shown in Table 12.

K Comparison with graph neural networks

The hypergraph could incorporate more information than a graph with binary edges theoretically, as the hyperedge denotes a set of nodes in graphs, which means the graph can be treated as a special case of hypergraph as shown in Fig. 7 (a). To further elaborate on the features and advantages of the hypergraph neural network architecture we use, we show the difference between our model and the graph neural network in this section, using 5 linear arranged nodes as an example in Fig. 7 (b)-(d). The black lines indicate the edges in the origin graph. This structure can correspond to the heavy atoms of the molecule malononitrile (NC-CH_2-CN). We focus on the message passing from the orange node to the green node in the graph. For a graph neural network, such message passing requires 4 layers. For the graph neural network with the addition of 3-hop node virtual edges, 2 layers are required. For SE3Set, on the other hand, only 2 layers are needed using the explicit overlap method, and only 3 layers are needed for the implicit overlap method, even in the case where the 3-hop nodes are not included inside the hyperedges either. This demonstrates the efficiency of SE3Set in message passing.

L Fragmentation method compared to BRICS

In order to demonstrate the difference of our proposed fragmentation method compared to previous methods like BRICS more clearly and intuitively, we use ethylene glycol diacetate as an example molecule for illustration in this section (shown in Figure 8). To directly show the difference we choose the explicit overlap method. Our fragmentation method preserves the predefined functional cluster substructure and generates overlaps between fragments to achieve message passing between different hyperedges in the hypergraph structure, whereas BRICS does not generate overlaps, which results in the hypergraph structure directly corresponding to BRICS not being able to In addition, BRICS generates molecular fragments based on a chemical reaction library that determines whether to break chemical bonds or not, which may lead to incomplete functional groups in fragments, such as the carboxyl group in this case.

M Summary Statistics

To further evaluate the performance in our different runs on different targets, we defined the summary statistics std. MAE following Gasteiger et al. (2019) which reflects the average error compared to the standard

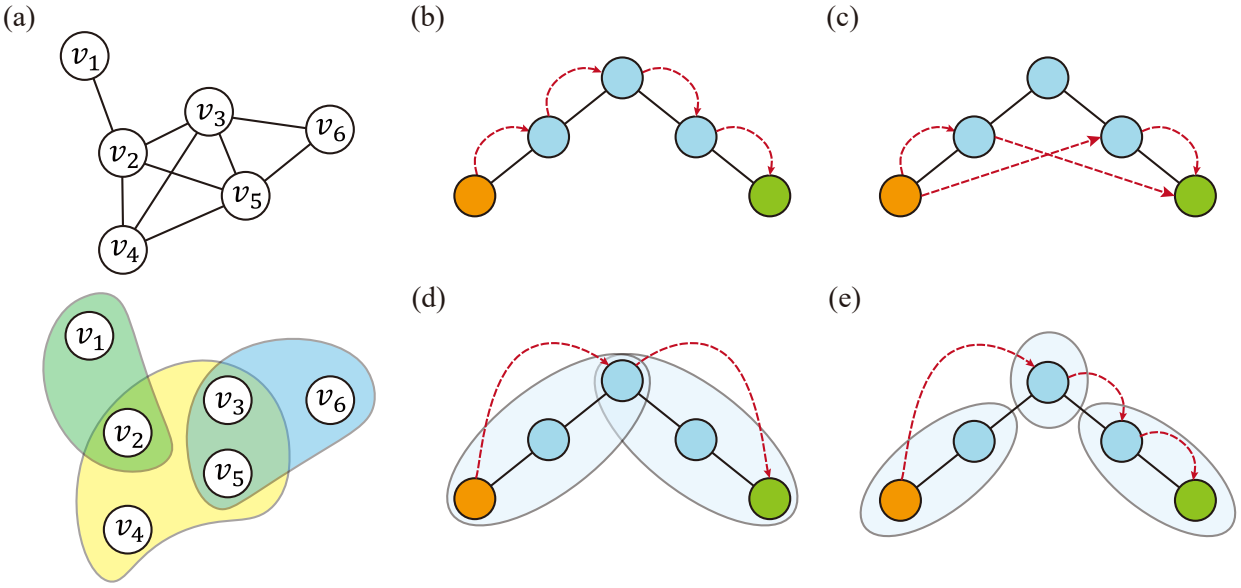

Figure 7: Comparison message passing efficiency of with GNN (graph neural networks), and the GNN adding virtual bodes between 3-hop neighborhoods. The black line between the two circles denotes the binary edge in the graph. We consider the message passing process from the orange node to the green node and the nodes in the shaded area belong to the same hyperedge. The red dashed arrows indicate the nodes where the source information reaches after each passing layer. (a) The structural differences between graph (above) and hypergraph (below). The hypergraph contains hyperedges defined by a set of nodes. (b) Simple GNN architecture. (c) The GNN architecture adding virtual bodes between 3-hop neighborhoods. (d) The hypergraph in SE3Set built with explicit overlap method. (e) The hypergraph in SE3Set built with implicit overlap method.

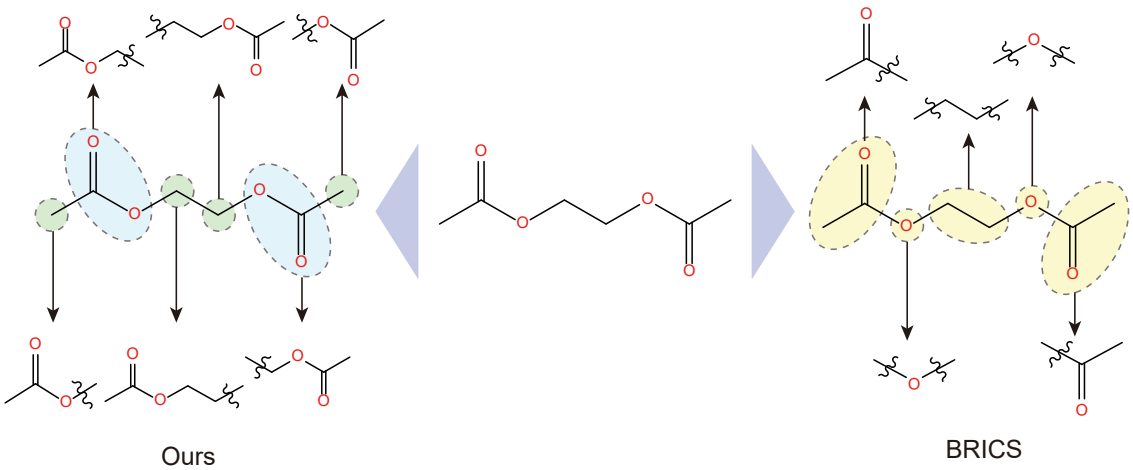

Figure 8: The difference between the proposed fragmentation method (left) and BRICS (right) shown by case molecule ethylene glycol diacetate. For convenience, we use an explicit fragmentation method and set the minimum number of atoms $n_{\min}$ to 0.

deviation of each target by Eq. 43,

$$\text{std. MAE} = \frac{1}{M}\sum_{m=1}^{M}\left(\frac{1}{N}\sum_{i=1}^{N}\frac{|\hat{y}_i^{(m)} - y_i^{(m)}|}{\sigma_m}\right) \tag{43}$$

with target index m in total M targets, dataset size N, the predict value of the model trained by m-th target, and the corresponding ground truth $y_i^{(m)}$.

Furthermore, to evaluate the robustness of the performance, especially the MAE, we further propose std. MAE std. by Eq. 44, which reflects the degree of data volatility of MAE on different tasks.

$$\text{std. MAE std.} = \sqrt{\frac{1}{M}\sum_{m=1}^{M}\left(\frac{1}{N}\sum_{i=1}^{N}\frac{|\hat{y_i}^{(m)} - y_i^{(m)}|}{\sigma_m} - \text{std. MAE}\right)} \tag{44}$$

We compute these metrics on QM9 ($M = 12$), MD17 ($M = 7$) and MD22 ($M = 5$) respectively. The OE62 is ignored as there is only one task in its experiment. For some energy-related labels (U_0, U, H, G) in QM9, the atomic level reference energy is subtracted from the origin value to generate the ground truth. For MD17 and MD22 datasets, as the forces are calculated by the derivation of energy, which means the energy MAE and force MAE belong to the same trained model, we calculate the metrics of energy and force separately with different molecules as different targets. All the results are shown in Table 13. To present the results more clearly, we also show the average value and standard deviation of the origin ground truth as well, which are presented in Table 14, 15, 16.

Table 13: The std. MAE and std. MAE std. of different datasets calculated across different targets.

dataset	QM9	MD17		MD22	
		Energy	Force	Energy	Force
std. MAE (%)	0.67	1.88	0.28	0.64	0.20
std. MAE std. (%).	0.82	0.28	0.13	0.12	0.05

Table 14: The average ground truth and standard deviation for different targets in the QM9 dataset.

Target	μ	α	HOMO	LUMO	gap	R^2	ZPVE	U_0	U	H	G	C_v
Unit	D	a_0^3	eV	eV	eV	a_0^2	eV	eV	eV	eV	eV	$\frac{\text{kcal}}{\text{mol}\cdot\text{K}}$
Avg.	2.7061	75.1917	-6.5300	0.3027	6.8328	1189.5256	4.0415	-75.9233	-76.3839	-76.8206	-70.6561	31.6009
Std.	1.5304	8.1876	0.6022	1.2772	1.2931	279.7507	0.9054	10.3775	10.4693	10.5440	9.5490	4.0624

Table 15: The average ground truth and standard deviation for different molecules in the MD17 dataset. Energy (E) is in unit of kcal/mol and force (F) is in unit of kcal/(mol $\cdot$ Å).

Molecule	Aspirin	Ethanol	Malonaldehyde	Naphthalene	Salicylic Acid	Toluene	Uracil
E Avg.	-406737.2765	-97195.9314	-167501.8334	-241898.7881	-311033.7587	-170223.8472	-260107.3102
E Std.	5.9468	4.1920	4.1399	5.5867	5.4163	5.0996	4.9230
F Avg.	0.0000	0.0002	0.0000	-0.0001	0.0000	0.0000	0.0000
F Std.	27.9284	26.2570	28.6374	28.6544	28.5897	27.3297	30.0238

Table 16: The average ground truth and standard deviation for different molecules in the MD22 dataset. Energy (E) is in unit of kcal/mol and force (F) is in unit of kcal/(mol $\cdot$ Å).

Molecule	Ac-Ala3-NHMe	DHA	Stachyose	AT-AT	AT-AT-CG-CG
E Avg.	-620662.7117	-631480.1418	-1578838.9203	-1154896.6603	-2329950.4156
E Std.	8.2038	9.5559	13.7595	10.9584	15.7047
F Avg.	0.0000	0.0000	0.0000	0.0000	0.0000
F Std.	26.0387	25.9614	25.6038	27.9251	27.7151